Interrogation and validation of the interactome of neuronal Munc18-interacting Mint proteins with AlphaFold2

Received for publication, September 20, 2023, and in revised form, November 27, 2023 Published, Papers in Press, December 9, 2023,
https://doi.org/10.1016/j.jbc.2023.105541

Saroja Weeratunga[1], Rachel S. Gormal[2], Meihan Liu[1], Denaye Eldershaw[1], Emma K. Livingstone[1], Anusha Malapaka[2], Tristan P. Wallis[2], Adekunle T. Bademosi[2], Anmin Jiang[2], Michael D. Healy[1], Frederic A. Meunier[2,3], and Brett M. Collins[1,*]

From the [1]Institute for Molecular Bioscience, [2]Clem Jones Centre for Ageing and Dementia Research, Queensland Brain Institute, and [3]School of Biomedical Sciences, The University of Queensland, Queensland, Australia

Reviewed by members of the JBC Editorial Board. Edited by Phyllis Hanson

Munc18-interacting proteins (Mints) are multidomain adaptors that regulate neuronal membrane trafficking, signaling, and neurotransmission. Mint1 and Mint2 are highly expressed in the brain with overlapping roles in the regulation of synaptic vesicle fusion required for neurotransmitter release by interacting with the essential synaptic protein Munc18-1. Here, we have used AlphaFold2 to identify and then validate the mechanisms that underpin both the specific interactions of neuronal Mint proteins with Munc18-1 as well as their wider interactome. We found that a short acidic α-helical motif within Mint1 and Mint2 is necessary and sufficient for specific binding to Munc18-1 and binds a conserved surface on Munc18-1 domain3b. In Munc18-1/2 double knockout neurosecretory cells, mutation of the Mint-binding site reduces the ability of Munc18-1 to rescue exocytosis, and although Munc18-1 can interact with Mint and Sx1a (Syntaxin1a) proteins simultaneously *in vitro*, we find that they have mutually reduced affinities, suggesting an allosteric coupling between the proteins. Using AlphaFold2 to then examine the entire cellular network of putative Mint interactors provides a structural model for their assembly with a variety of known and novel regulatory and cargo proteins including ADP-ribosylation factor (ARF3/ARF4) small GTPases and the AP3 clathrin adaptor complex. Validation of Mint1 interaction with a new predicted binder TJAP1 (tight junction–associated protein 1) provides experimental support that AlphaFold2 can correctly predict interactions across such large-scale datasets. Overall, our data provide insights into the diversity of interactions mediated by the Mint family and show that Mints may help facilitate a key trigger point in SNARE (soluble *N*-ethylmaleimide-sensitive factor attachment receptor) complex assembly and vesicle fusion.

Synaptic vesicle fusion and release of neurotransmitters requires the formation of specific complexes between vesicular and plasma membrane SNARE proteins (soluble *N*-ethylmaleimide-sensitive factor attachment receptors). The vesicular v-SNAREs and target t-SNAREs form an α-helical coiled-coil assembly that provides the necessary energy to bring the two opposing lipid membranes together for membrane fusion. Munc18-1 (also called Munc18a, syntaxin-binding protein 1 [STXBP1], and neuronal Sec1 [nSec1]) is a member of the Sec1/Munc18 (SM) protein family and an essential regulatory protein required for the assembly of this SNARE complex in neuronal membrane fusion. Munc18-1 binds with high affinity to the target or Qa-SNARE Syntaxin1a (Sx1a) and mediates both its trafficking and its incorporation into the SNARE complex with the Qbc-SNARE SNAP25 and the vesicle or R-SNARE Vamp2.

Importantly, Munc18-1 also interacts with other regulatory proteins including Munc13 and the two Munc-interacting protein (Mint) paralogs, Mint1 and Mint2. Mints (also known as X11, amyloid precursor protein [APP]-binding family A [APBA] or Lin-10 proteins) are multidomain scaffolds that participate in a host of protein–protein interactions. The human genome encodes three Mint homologs, Mint1, Mint2, and Mint3 (1) (Fig. 1*A*). Mint1 and Mint2 are highly enriched in brain and spinal cord tissue, whereas Mint3 is ubiquitously expressed (2-6). Structurally, Mint proteins are composed of conserved C-terminal phosphotyrosine binding (PTB) and tandem PDZ domains and possess highly extended intrinsically disordered N-terminal domains that mediate paralog-specific interactions. As scaffold proteins, the PTB domains of the Mint proteins interact with various ligands containing NPxY sequences (x is any amino acid) such as the APP, APP-like proteins APLP1 and APLP2, and TrkA (7-18), whereas the PDZ domains of the Mint proteins bind to C-terminal PDZ binding motifs (PDZbms) in molecules including *N*-methyl-D-aspartate (NMDA) receptors, kalirin-7, neurexins, ApoER2, and LDLR (19-23). The N termini of the Mint proteins contain sequences that mediate both conserved and isoform-specific protein–protein interactions; for example, an N-terminal sequence specific to Mint1 called the Ca^{2+}/calmodulin-dependent serine protein kinase (CASK)-interacting domain (CID) binds specifically to CASK/Lin-2 (a multidomain adapter and Mg^{2+}-independent S/T kinase) forming a tripartite complex with Veli/Lin-7 family proteins and neurexins at the presynapse (8, 24-27). In contrast, the N-terminal regions of Mint1 and Mint2 proteins can both

* For correspondence: Brett M. Collins, b.collins@imb.uq.edu.au.

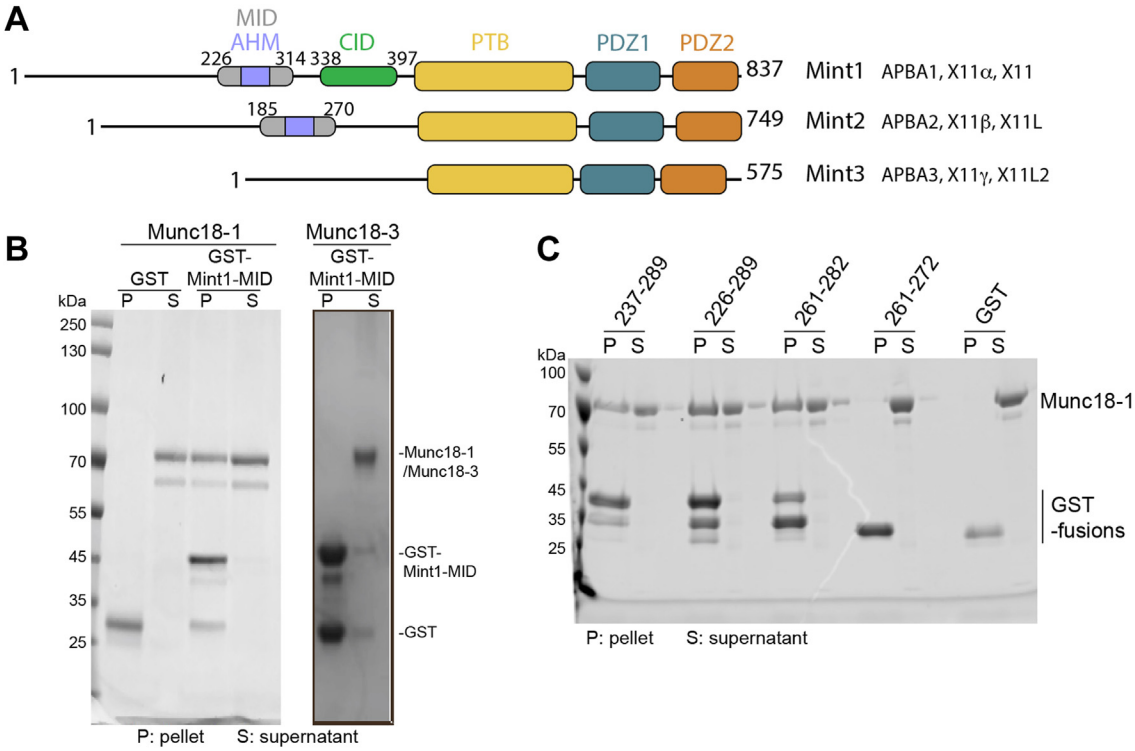

Figure 1. The Mint1 MID interacts directly with Munc18-1 but not Munc18-3. *A*, schematic diagram of the human Mint proteins. *B*, pulldowns with GST-Mint1 MID show a direct interaction with purified Munc18-1 but not Munc18-3. Image shows Coomassie blue–stained gel. *C*, pulldowns with GST-tagged Mint1-truncated sequences identify residues 261 to 282 as sufficient and required for Munc18-1 binding. Image shows Coomassie blue–stained reducing SDS-PAGE gels. AHM, acidic α-heilcal motif; CID, CASK-interacting domain; GST, glutathione-*S*-transferase; MID, Munc18-1-interacting domain; Mint, Munc18-interacting protein; PTB, phosphotyrosine binding domain.

interact with Munc18-1 *via* a sequence termed the Munc18-1-interacting domain (MID) (3, 19, 28-32). However, until recently, the mechanism of Munc18-1 interaction was unknown.

The importance of Mint proteins in neuronal function is apparent in studies showing that homozygous deletions of Mint1 or Mint2 display disrupted GABAergic transmission (33, 34), whereas knockout of both Mint1 and Mint2 neuronal isoforms leads to lethality at birth in most animals, with surviving mice displaying deficits in motor behaviors and spontaneous neurotransmitter release. A prominent phenotype of knockout animals is an alteration in APP trafficking and processing to the Alzheimer's plaque peptide amyloid β (15, 35), although the changes appear to be dependent on specific knockout conditions with both an increase (34, 36, 37) and decrease (11, 15) in amyloid β production reported. Thus, the molecular interactions between Mints, synaptic proteins, and trafficking partners involved in neurodegenerative diseases is of broad interest to the field.

Mutations in the core neuronal presynaptic machinery including Munc18-1 and Sx1a lead to a distinct but overlapping set of neurodevelopmental disorders, with symptoms including neurodevelopmental delay, intellectual disability, and early infantile epileptic encephalopathy (38, 39). Mutations in the Mint1-associated CASK protein have also been found to cause neurodevelopmental disorders with similar features, including mental retardation and microcephaly with ophthalmic atrophy (40-43), and the human disease–linked missense variant p.Leu209Pro in CASK linked to optic nerve hypoplasia specifically disrupts Mint1 binding without impacting other protein interactions (42). Mutations in the Mint proteins themselves have not yet been specifically linked to similar disorders, although copy number variations in Mint2 have been described in patients with epilepsy and intellectual disability (44). In addition, variants in Mint2 have been linked to autism spectrum disorder, potentially through disruption of neurexin trafficking (45, 46). By assessing the mechanisms responsible for Mint1 binding to a range of protein partners, we aim to provide a framework that can contribute to the understanding of how Mint1 might modulate a role during neurotransmission and trafficking.

Here, we explored the use of AlphaFold2 to identify and predict the structural basis for Mint protein interactions across their putative interactome. We initially focused on the interaction with SNARE regulatory protein Munc18-1, where AlphaFold2 confidently predicts a direct association with Mint1 and Mint2 and extensively validate the mechanism of binding between the Mint MID and a novel binding site in domain 3b of Munc18-1. We define a minimal short linear interaction motif of 13 amino acids in Mint1 and Mint2 that is required and sufficient for Munc18-1 interaction. The AlphaFold2-derived model of the Mint1 and Mint2 sequences bound to Munc18-1 shows that the peptides form an acidic α-helical motif (AHM) bound to Munc18-1 domain 3b. Providing further evidence for the ability of AlphaFold2 to accurately predict novel protein–peptide complexes, while this

was predicted and validated prior to any experimental structure, recent work by Li *et al.* (47) described a crystal structure revealing an essentially identical association. Munc18-1 mutation R388A blocks Mint-1 interaction *in vitro* and significantly reduced the number of exocytic events detected using VAMP2-pHluorin unquenching in Munc18-1/2 double knockout (DKO) PC12 cells. Although the respective Mint1/2- and Sx1a-binding sites in domain 3b and domains 1/3a are distinct from each other, their individual Munc18-1 *in vitro* binding affinities are reduced in the presence of the other ligand. We speculate that this antagonistic allosteric interaction between the two proteins may be important for regulating Munc18-1 templating of SNARE complex formation. Building on the successful structural predictions of Mint1 and Munc18-1 with AlphaFold2, we have explored the wider network of interactions mediated by the Mint scaffolds. We confidently identify a novel binding site in the Mint PDZ domains for ARF small GTPases and experimentally validate a noncanonical site in the Mint PTB domain, distinct from the NPxY peptide motif–binding site, which mediates binding to tight junction–associated protein 1 (TJAP1). These studies provide an overall model for neuronal Mint1 and Mint2 assembly with both effector and regulatory proteins.

Results

Mapping the Munc18-1-binding sequence of Mint1 and Mint2

A number of studies have shown that both Mint1 and Mint2 homologs can interact with Munc18-1, using methods including immunoprecipitation and yeast two-hybrid assays (3, 19, 30, 48, 49). Mint proteins are multidomain scaffolds with a C-terminal PTB domain and tandem PDZ domains preceded by a long and unfolded N-terminal sequence that shows low sequence homology across the family (Figs. 1*A* and S1). Munc18-1 binding has been mapped by yeast two-hybrid assays to a region termed the MID within the N terminus of the neuronal Mint1 and Mint2 proteins consisting of residues 226 to 314 and 185 to 270, respectively (30). We first confirmed the direct interaction of Mint1 with purified Munc18-1, performing a glutathione-*S*-transferase (GST) pull-down assay using the human Mint1 MID as bait (residues 222–314). This showed clear binding between the two proteins that was specific for the neuronal Munc18-1 protein as we did not detect any interaction with Munc18-3 (Fig. 1*B*). As the entire N terminus of Mint1 including the MID is expected to be unstructured in isolation, we hypothesized that Munc18-1 may be binding to a shorter peptide sequence or short linear interaction motif (50) within the MID. To test this, we generated several truncated Mint1 MID sequences and tested their binding to Munc18-1 by GST pull-down assay (Fig. 1*C*). This showed that a 21 amino acid region encompassing residues 261 to 282 was required and sufficient for Munc18-1 binding.

The binding of a synthetic Mint1 peptide to Munc18-1 was next measured by isothermal titration calorimetry (ITC), and the affinity (K_d) of the interaction was found to be 16.3 ± 4.2 μM (Fig. 2, *A* and *B* and Table 1), which is similar to recent reports (47). With a direct assay for Mint1 (261–282) peptide interaction, we generated a series of N- and C-terminal deletions and found that the minimal binding sequence for Munc18-1 in human Mint1 consists of the 13 residues from Glu267 to Ser280 (Figs. 2*B* and S2; Table 1). This region is notably the most highly conserved sequence in the N terminus of Mint1 and Mint2 across species (Fig. S1). In line with this, we also find that an overlapping peptide from human Mint2 shares a similar binding affinity for Munc18-1 (Figs. 2*B* and S2; Table 1). Within this region, the sequence ^{267}EEDIDQIVAE^{276} is invariant across Mint1 and Mint2 homologs from human, fish, and xenopus species, although it is not present in worms and flies (Fig. S1), and a series of double alanine substitutions in this sequence showed that all these residues are important for Munc18-1 interaction by ITC (Figs. 2*B* and S2; Table 1). The conservation of this minimal binding sequence suggests

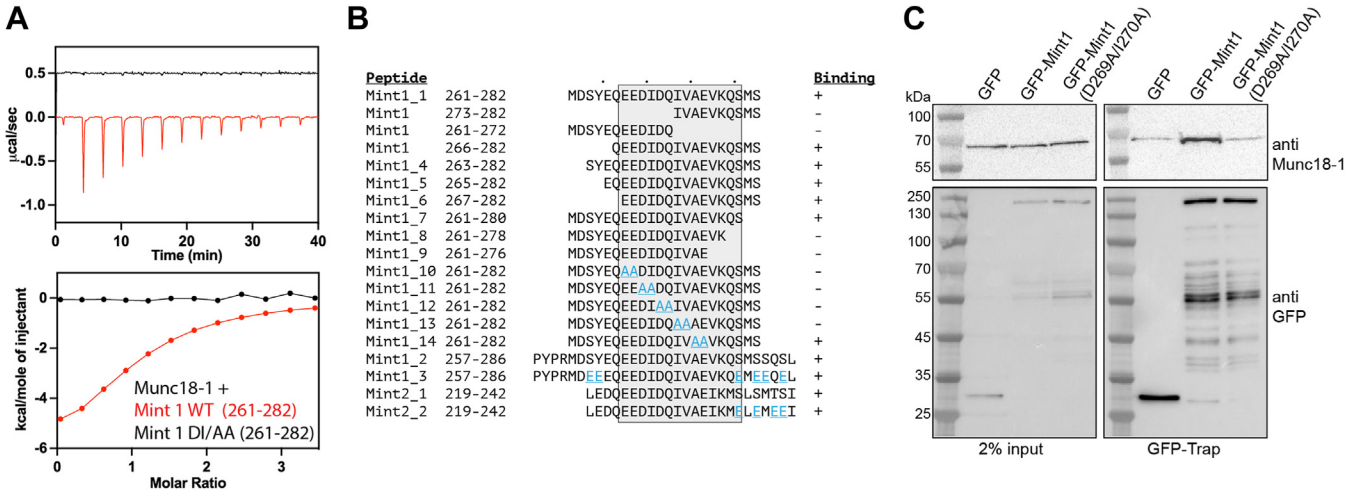

Figure 2. A conserved sequence in Mint1 and Mint2 binds Munc18-1 and is not influenced by phosphorylation. *A*, ITC of synthetic Mint1$^{261–282}$ peptide binding to purified Munc18-1. The *top* shows raw ITC data, and the *bottom* shows integrated and normalized data fit to a 1:1 binding model. *B*, sequences of peptides tested for Munc18-1 binding by ITC. The minimal and highly conserved sequence required for Munc18-1 binding is *shaded*. Mutated peptide residues are highlighted in *blue*. *C*, endogenous Munc18-1 is bound to GFP-tagged Mint1 but not the mutant GFP-Mint1$^{D269A/I270A}$. GFP-tagged Mint1 proteins were transiently transfected into PC12 cells, immunoprecipitated with GFP-nanobody–coupled beads, and the bound proteins probed by Western blot with anti-Munc18-1. ITC, isothermal titration calorimetry; Mint, Munc18-interacting protein.

Table 1
Thermodynamic parameters of Munc18-1 binding to Mint1 by ITC

Syringe sample	Peptide residues	Peptide sequences	K_d (μM)	N	ΔH (kcal/mol)	$-T\Delta S$ (kcal/mol)	ΔG (kcal/mol)
Mint1_1	261–282	MDSYEQEEDIDQIVAEVKQSMS	16.3 ± 4.2	0.8	−8.8 ± 0.6	2.8 ± 1.2	−6.5 ± 0.1
Mint1_1a	273–282	IVAEVKQSMS	Nb				
Mint1_1b	261–272	MDSYEQEEDIDQ	Nb				
Mint1_1c	266–282	QEEDIDQIVAEVKQSMS	23.1 ± 1.9	1	−1.2 ± 0.2	−5.4 ± 0.2	−6.39 ± 0.01
Mint1_4	263–282	SYEQEEDIDQIVAEVKQSMS	12.9	1.3	−2.30	−4.38	−6.70
Mint1_5	265–282	EQEEDIDQIVAEVKQSMS	5.6	1.3	−3.48	−3.69	−7.17
Mint1_6	267–282	EEDIDQIVAEVKQSMS	4.0	1.2	−1.29	−6.08	−7.37
Mint1_7	261–280	MDSYEQEEDIDQIVAEVKQS	19.1	1	−1.78	−4.67	−6.44
Mint1_8	261–278	MDSYEQEEDIDQIVAEVK	Nb				
Mint1_9	261–276	MDSYEQEEDIDQIVAE	Nb				
Mint1_10	261–282 E267A/E268A	MDSYEQ**AA**DIDQIVAEVKQSMS	Nb				
Mint1_11	261–282 D269A/I270A	MDSYEQEE**AA**DQIVAEVKQSMS	Nb				
Mint1_12	261–282 D271A/Q272A	MDSYEQEEDI**AA**IVAEVKQSMS	Nb				
Mint1_13	261–282 I273A/V274A	MDSYEQEEDIDQ**AA**AEVKQSMS	Nb				
Mint1_14	261–282 A275A/E276A	MDSYEQEEDIDQIV**AA**VKQSMS	216	1.0	−57.6	52.6	−5.00
Mint1_2	257–286	PYPRMDSYEQEEDIDQIVAEVKQSMSSQSL	26.0	**1.3**	−4.21	−3.41	−7.62
Mint1_3	257–286 phosphomimic	PYPRMD**EE**EQEEDIDQIVAEVKQ**E**M**EE**Q**E**L	14.0	1.1	−6.5	−0.103	−6.60
Mint2_2	219–242 phosphomimic	LEDQEEDIDQIVAEIKM**E**L**E**M**EE**I	200	1	−17.2	12.2	−5.05

Bold and underlined amino acids denote mutated residues in these synthetic peptide sequences.
Abbreviation: Nb, No binding detected.

that Munc18-1 interactions with Mint1 and Mint2 plays a critical role in the functions of these proteins.

We confirmed the binding of Mint1 to endogenous Munc18-1 in PC12 cells by coimmunoprecipitation (co-IP). GFP-Mint1 or GFP-Mint1 (D269A/I270A) were expressed in PC12 cells and bound to GFP-nanotrap beads followed by blotting for the presence of Munc18-1 (Fig. 2*C*). The mutation D269A/I270A reduced Munc18-1 binding in agreement with our *in vitro* ITC data.

Phosphomimetic Mint1 mutations do not affect the binding to Munc18

The N-terminal region of Mint1 and Mint2 is predicted to be unstructured and can be phosphorylated at numerous sites as cataloged in the PhosphoSitePlus database (51) (Fig. S3*A*). There are several potential sites of Ser/Thr phosphorylation adjacent to the minimal Munc18-1 binding sequences of Mint1 and Mint2 (Fig. S3*B*). Given the overall negative electrostatic charge distribution of the Mint1 and Mint2 N-terminal domains (Fig. S3*C*), we speculated that adding further negative charges in the form of phosphorylation might influence the affinity of the Munc18-1 interaction. We designed two longer peptides of Mint1 and Mint2 with putative phosphorylated residues altered to phosphomimetic glutamic acid side chains and tested their binding by ITC (Figs. 2*B* and S2; Table 1). Our results suggest that phosphorylation of Mint proteins near to the Munc18-interacting sequence does not play a direct role in modulating the Munc18-1 binding affinity at least *in vitro*, although we cannot rule out that Glu is an imperfect mimic of phosphorylation. Previous studies showed that Mint1 and Mint2 N-terminal domains can be phosphorylated upstream of the Munc18-1-interacting sequence by the tyrosine kinase c-Src (52). While this enhanced the trafficking of APP *via* binding the PTB domain, presumably by affecting the overall conformation of Mint1, it had no effect on Munc18-1 interaction. Phosphorylation of Ser236 and Ser238 in Mint2 also enhances the APP interaction (14). These sites lie directly adjacent to the Munc18-1-interacting sequence, but our ITC experiments indicate they do not affect Munc18-1 binding (Figs. 2*B* and S2; Table 1). Therefore, it appears that while phosphorylation-dependent regulation of the Mint1 N-terminal region plays a role in the interactions with APP (and likely other PTB domain–binding transmembrane proteins such as APLP1, APLP2, Megalin, and LRP), they are dispensable for Munc18-1 association *in vitro*.

Mint1 forms an acidic AHM that binds to Munc18-1 domain 3b

The machine-learning structure-prediction algorithm AlphaFold2 (53, 54) has been successfully used to predict structures of protein–peptide complexes by ourselves and others (55-58). We began our analyses of Mint interactions with a series of modeling experiments to map the complex between Munc18-1 and Mint1 using the ColabFold implementation of AlphaFold2 (59). We initially predicted the complex between the Mint1 and Munc18-1 full-length proteins (Fig. S4*A*). Across multiple models, we assessed (i) the prediction confidence measures (pLDDT and interfacial post-translational modification [PTM] scores), (ii) the plots of the predicted alignment errors (PAEs), and (iii) backbone alignments of the final structures. This identified a high-confidence binding sequence in the N-terminal region of Mint1 that correlated precisely with the binding motif identified in our biochemical experiments (Fig. S4*A*).

Based on this initial model and our biochemical mapping of the minimal Mint1 sequence for Munc18-1 binding, we performed multiple independent predictions using a shorter peptide region, combined with AMBER energy minimization to optimize amino acid stereochemistry. We found that the minimal sequence of Mint1 was invariably predicted to form an extended α-helical structure that associated with the Munc18-1 domain 3b (Fig. 3, *A* and *B*). This novel binding site is highly conserved in Munc18-1, to a similar degree to the binding site for the Sx1a SNARE protein (Fig. 3*C*). In addition, we found that both the human Munc18-1 and Mint2 proteins and the zebrafish Munc18-1 and Mint1 orthologs were consistently predicted to form identical structures (Fig. S4, *B* and *C*). In contrast, the human Munc18-3 protein was not predicted to form a stable complex with Mint1 (Fig. S4*D*)

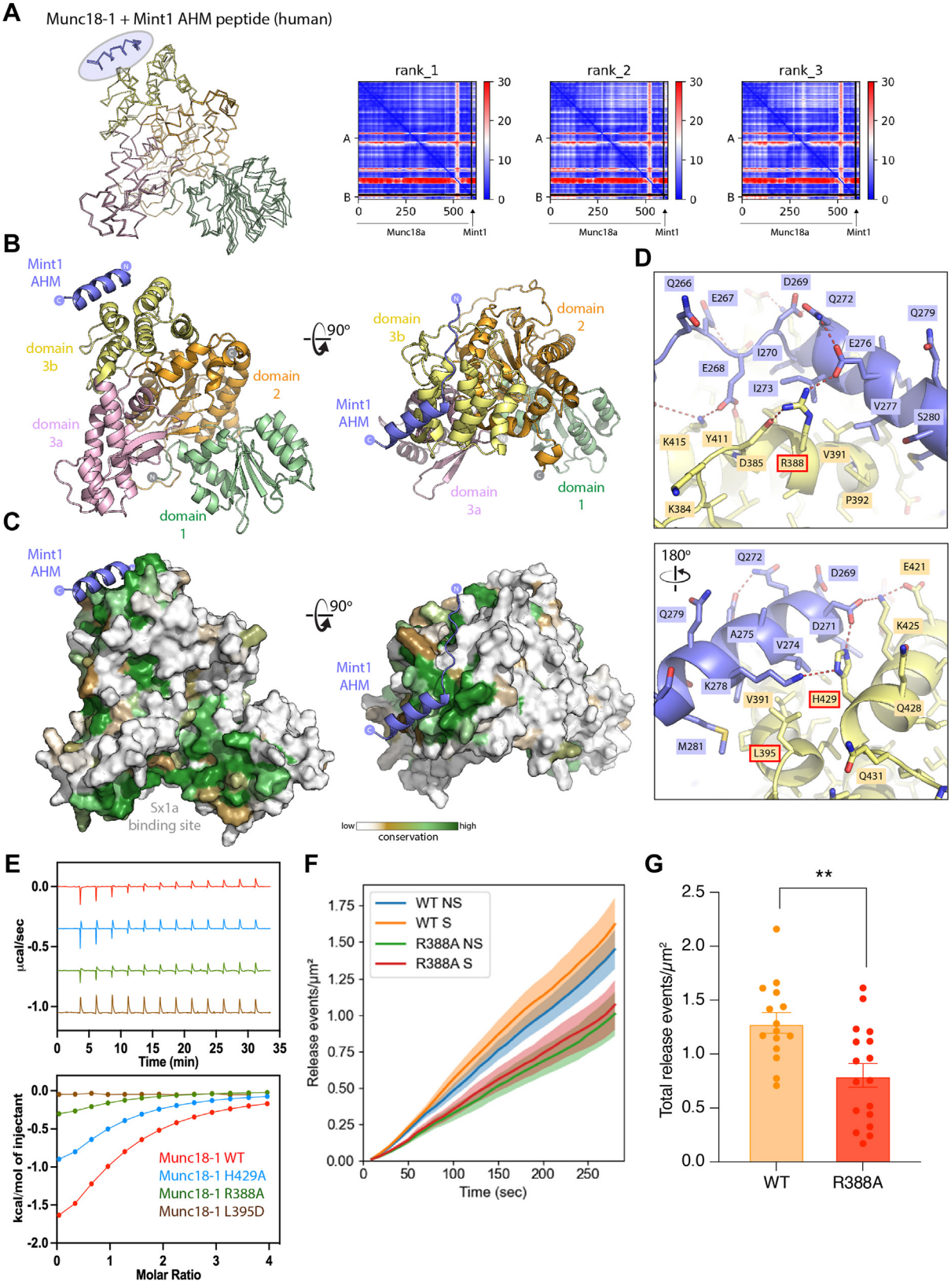

Figure 3. Modeling of Munc18-1 in complex with the Mint1 AHM sequence. *A*, AlphaFold2 prediction of the complex between Munc18-1 and Mint1 AHM. The three top ranked models are overlaid and shown in *backbone ribbon* representation. The AHM is consistently modeled in an α-helical structure associated with the Munc18-1 domain3b (highlighted in *blue*). On the *right*, the predicted alignment error (PAE) is plotted for each model. Signals in the off-diagonal regions indicate strong structural correlations between residues in the peptide with the Munc18-1 protein. Fig. S4 shows predictions of the full-length Munc18-1 and Mint1 complex as well as models of other Munc and Mint homologs and orthologs. *B*, the top-ranked complex of Munc18-1 and the Mint1 AHM is shown in *cartoon* representation, with Munc18-1 domains highlighted. *C*, as in (*B*), but the surface of Munc18-1 is shown colored for sequence conservation as calculated by ConSurf (120). Movie S1 shows an animation of the structure and its key features. *D*, opposite views showing details of the

consistent with their lack of interaction *in vitro* (Fig. 1*B*). Finally, we modeled the tripartite interaction of human Munc18-1 and CASK with an extended Mint1 sequence containing both the Munc18 and CID (Fig. S4*E*). The two Mint1 regions were modeled by AlphaFold2 to bind their respective partners in the expected conformations, with the CASK-binding sequence matching closely in structure to the previous crystal structures of the CASK–Mint complex (26, 27).

The Mint1-interacting sequence forms what we refer to as an acidic AHM as proposed by Li *et al.* (47) (see later) and makes a number of critical contacts with Munc18-1 domain3b including both hydrophobic and electrostatic interactions between conserved side chains (Fig. 3*D* and Movie S1). Consistent with our truncation and mutation analyses of the Mint1 MID peptides (Fig. 2*B*), all predicted core contacts with Munc18-1 are mediated by Mint1 AHM residues Glu262-Ser280. Toward the N terminus of Mint1, acidic Glu267, Glu268, Asp269, and Glu276 each form complementary bonds with Munc18-1 residues, most notably with Arg388, Tyr411, and Lys415. These are supported by buried hydrophobic interactions of Mint1 Ile270 and Ile273. On the opposite side of the Mint1 α-helix C terminus, a network of bonds is formed between Mint1 Asp271 and Lys278, with Glu421, Lys425, and His429 of Munc18-1. To confirm the predicted binding site of Mint1 and Mint2, we mutated several residues in domain 3b of Munc18-1, including R388A, L395D, and H429A. In ITC experiments, all three mutations showed a reduction in binding affinity and enthalpy, with L395D showing an almost complete loss of association (Fig. 3*E*). Altogether, the Mint1 AHM is predicted to form an extensive complementary interface with Munc18-1, and we speculate that the relatively modest affinity between the two proteins may in part be due to the entropic cost of the induced α-helical folding of the AHM sequence.

To test the functional importance of this interaction for Munc18-1-dependent exocytosis in neurosecretory cells, we performed an exocytic release assay using Munc18-1/2 DKO PC12 cell line in rescue conditions (60). We measured exocytic events by total internal reflection fluorescence (TIRF) microscopy in DKO-PC12 cells cotransfected with VAMP2-pHluorin and either Munc18-1^{WT}-mEos3.2 or Munc18-1^{R388A}-mEos3.2—a mutation blocking Mint-1 interaction. VAMP2-pHluorin is classically used to assess vesicular fusion as the intraluminal pH-sensitive pHluorin moiety undergoes unquenching upon exposure to the neutral extracellular environment. This unquenching can be used to study vesicle fusion events and assess the contribution of Munc18-1–Mint1 binding to exocytosis. To assess potential fusion events, we developed a custom Python pipeline that detected puncta of fluorescently labeled vesicles and assessed them over time. A representative cell shows the initiation and disappearance of several vesicles indicative of fusion events in 3D (time being the third axis) (Fig. S5). We found that the cells expressing the Mint1 binding–deficient Munc18-1^{R388A}-mEos3.2 showed a reduced number of exocytic events (Fig. 3*F*) and yielded an approximate 40% decrease in the number of evoked exocytic events relative to the level found upon re-expression of the WT protein (Fig. 3*G*).

The AlphaFold2-predicted interaction precisely matches the crystal structure of the Mint1–Munc18-1 complex

Despite attempts to crystallize Munc18-1 bound to various Mint1 peptides, we were unable to determine a high-resolution structure of this complex, including with stabilized Munc18-1 variants (61). However, as this work was being completed, the Song and Feng labs (47) published similar findings regarding the interaction of Munc18-1 with Mint proteins. The crystal structure of rat Mint1 (227–303) bound to a complex of Munc18-1 and Sx1a was resolved at 3.2 Å resolution, with electron density observed for Mint1 residues 266 to 283 associated with Munc18-1 domain 3b. This experimental structure correlates precisely with the region of human Mint1 we have mapped biochemically by truncations and mutagenesis and structurally with AlphaFold2. Based on their crystal structure, Li *et al.* termed the Munc18-1-binding Mint1 sequence the acidic AHM, and we have also adopted this terminology. Overlay of the Munc18-1–Mint1 crystal structure with the top-ranked AlphaFold2 model shows an essentially identical binding mode in all key details (Fig. 4*A*), and it is important to note the crystal structure was not included in the AlphaFold2 training set. One minor difference is that the AlphaFold2 predictions consistently model stable electrostatic contacts involving Mint1 Glu267 and Glu268. These are not seen in the crystal structure, and this is likely because these electrostatic interactions are relatively transient and thus not observed in the modest resolution electron density maps.

In addition to the crystal structure of Munc18-1/Sx1a bound to the Mint1 AHM, the structure of Munc18-1 was recently determined in a ternary complex with Sx1a and the vesicular R-SNARE VAMP2 (also known as synaptobrevin) by cryo-EM (62). Similar to what was observed for yeast SM-family protein Vps33, this showed that Munc18-1 can provide a platform to template the assembly of the Qabc-SNARE–R-SNARE complex required for membrane fusion (63). Overlay of the complexes shows that the Mint1- and VAMP2-binding sites do not overlap, and thus, Mint1 could potentially associate simultaneously with both SNARE proteins (Fig. 4*B*).

Mint1 binding to Munc18-1 allosterically modulates Sx1a interaction

Although the Mint-binding site on Munc18-1 does not overlap with either the known VAMP2- or Sx1a-binding sites, it is still possible that protein dynamics or allosteric effects

Mint1 AHM bound to the Munc18-1 domain3b. *E*, ITC of synthetic Mint1$^{261–282}$ peptide binding to purified Munc18-1 and structure-based mutants. The *top* shows raw ITC data, and the *bottom* shows integrated and normalized data fit to a 1:1 binding model. Mutated residues are highlighted in *D*. *F*, cumulative release events over time for each data group were analyzed, and the number of release events at each 10 s interval from 0 to 290 s was determined, plotted as mean ± SEM. *G*, total evoked release events following stimulation were measured per μm^2. Nonparametric Mann–Whitney *U* test, $p < 0.05$, *$p < 0.01$. N = 15 cells (WT) and 17 (R388A) from independent experiments. AHM, α-helical motif; ITC, isothermal titration calorimetry; Mint, Munc18-interacting protein; NS, nonstimulated; S, stimulated with 2 mM $BaCl_2$.

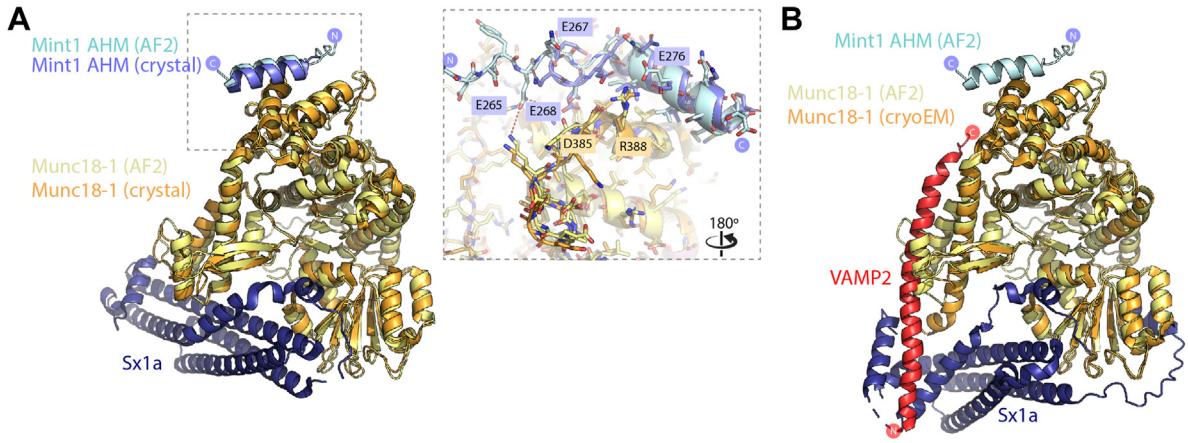

Figure 4. Comparison of the predicted Munc18-1–Mint1 complex with experimental structures. *A*, overlay of the Munc18-1 complex with Mint1 AHM predicted by AlphaFold2 and the recent crystal structure of the Munc18-1–Sx1a–Mint1 complex (47) (Protein Data Bank code: 7XSJ). The *inset* shows details of the binding site modeled by AlphaFold2 and observed in the crystal structure. The two structures are identical in all key respects. *B*, overlay of the Munc18-1 complex with Mint1 AHM predicted by AlphaFold2 and the cryo-EM structure of the Munc18-1–Sx1a–VAMP2 complex (62). The Mint1 AHM is expected to bind Munc18-1 independently of the Sxa1 t-SNARE and VAMP2 v-SNARE proteins. AHM, α-helical motif; Mint, Munc18-interacting protein; Sx1a, Syntaxin1a.

could be involved in Mint interaction. To partially address this question, we examined the impact of domain3a deletions and/or the presence of Sx1a on their binding. Previous studies have shown that the flexible hinge-loop region of Munc18-1 domain3a (residues 317–333) is required for efficient priming of secretory vesicles and controls the mobility of Sx1a and subsequent assembly of the SNARE complex (64-66). Structural studies of Munc18-1 show that this hinge-loop adopts a "closed" or inhibitory conformation when Munc18-1 is bound to the Sx1a Habc and SNARE domains (67, 68). Other structures of apo squid Munc18-1, rat Munc18-1 bound to a short Sx1a N-terminal peptide, and the recent cryo-EM structure of Munc18-1 in ternary complex with Qa-SNARE Sx1a and R-SNARE VAMP2 show that domain3a can also adopt an "open" conformation that is thought to be necessary for both releasing Sx1a inhibition and providing a platform for binding and assembly of other SNAREs (62, 69-71). This is similar to what is seen when yeast SM protein Vps33 is bound to the Nyv1 SNARE (63). Surprisingly, we find that deletion of the hinge-loop region in Munc18$^{\Delta 317-333}$, which has only a modest effect on Sx1a binding (64, 66), abolishes the binding of Mint1 both in GST pull-down and ITC experiments (Fig. 5, *A* and *B*).

As Mint1 binds to Munc18-1 domain 3b, we hypothesized that the perturbed Mint1 interaction on deletion of the distal domain 3a hinge-loop might be due to altered structural dynamics in the combined domain3a/3b module. We therefore tested the binding of Sx1a to Munc18-1 in the absence and presence of the Mint1$^{261-282}$ peptide to determine if there were any changes in Sx1a affinity because of allosteric interactions. By GST pulldown of GST-Mint1 MID, we did not observe a gross impact on the ability to bind Munc18-1 in the presence of the high-affinity Sx1a ligand (Fig. 5*C*). This is in line with the ability to cocrystallize the three proteins when excess Mint1 peptide is present (47). However, when we quantified the binding affinity by ITC in the presence of Sx1a, we saw a small but reproducible reduction in the affinity and enthalpy of binding of Mint1$^{261-282}$ peptide (Fig. 5*D* and Table 2). In reverse experiments, in the presence of a molar excess of Mint1$^{261-282}$ peptide, we observed a reciprocal reduction in Sx1a binding affinity (K_d) from 7.9 nM to 269 nM (Fig. 5*E* and Table 2). This reduced affinity for Sx1a caused by Mint1-dependent allostery is not seen when we use Mint-binding deficient Munc18$^{\Delta 317-333}$ as expected (Fig. 5*F* and Table 2). Overall, the data indicate that Sx1a and Mint1 binding to Munc18-1 domains 3a and 3b, respectively, can allosterically regulate the interaction of the other protein. This has potential implications for a role of Mint proteins in Munc18-1-mediated SNARE assembly, which is a tightly regulated and highly dynamic process.

Assessing the network of Mint interactions using AlphaFold2-based predictions

In parallel to the successful modeling of the interaction with Munc18-1/2, we also explored the potential of AlphaFold2 to screen for, and map the binding sites of, other protein–protein interactors of the Mint1 and Mint2 neuronal proteins. Putative Mint1 and Mint2 interactors from the BioGRID repository (72) were screened for direct complex formation with Mint1 and Mint2, respectively, using the ColabFold Batch implementation of AlphaFold2 (59) (Tables S1 and S2). To assign a direct "interactor" from these *in silico* analyses, we used an approach similar to recent work by Sifri *et al.* (73). We initially assessed both the AlphaFold2-derived interfacial PTM (iPTM) score and the resultant PAE graphs, which provide confidence metrics for the interactions between the proteins. For those with promising scores, we also examined the predicted structures in PyMOL to assess whether interacting regions involved the expected complementary hydrophobic, polar, and electrostatic contacts. We initially generated three independent predictions of each putative full-length complex in AlphaFold2 in unsupervised batch mode. We found that a minimum iPTM score of ∼0.3 combined with a strong signal in the PAE plots for intermolecular structural correlation typically provided a

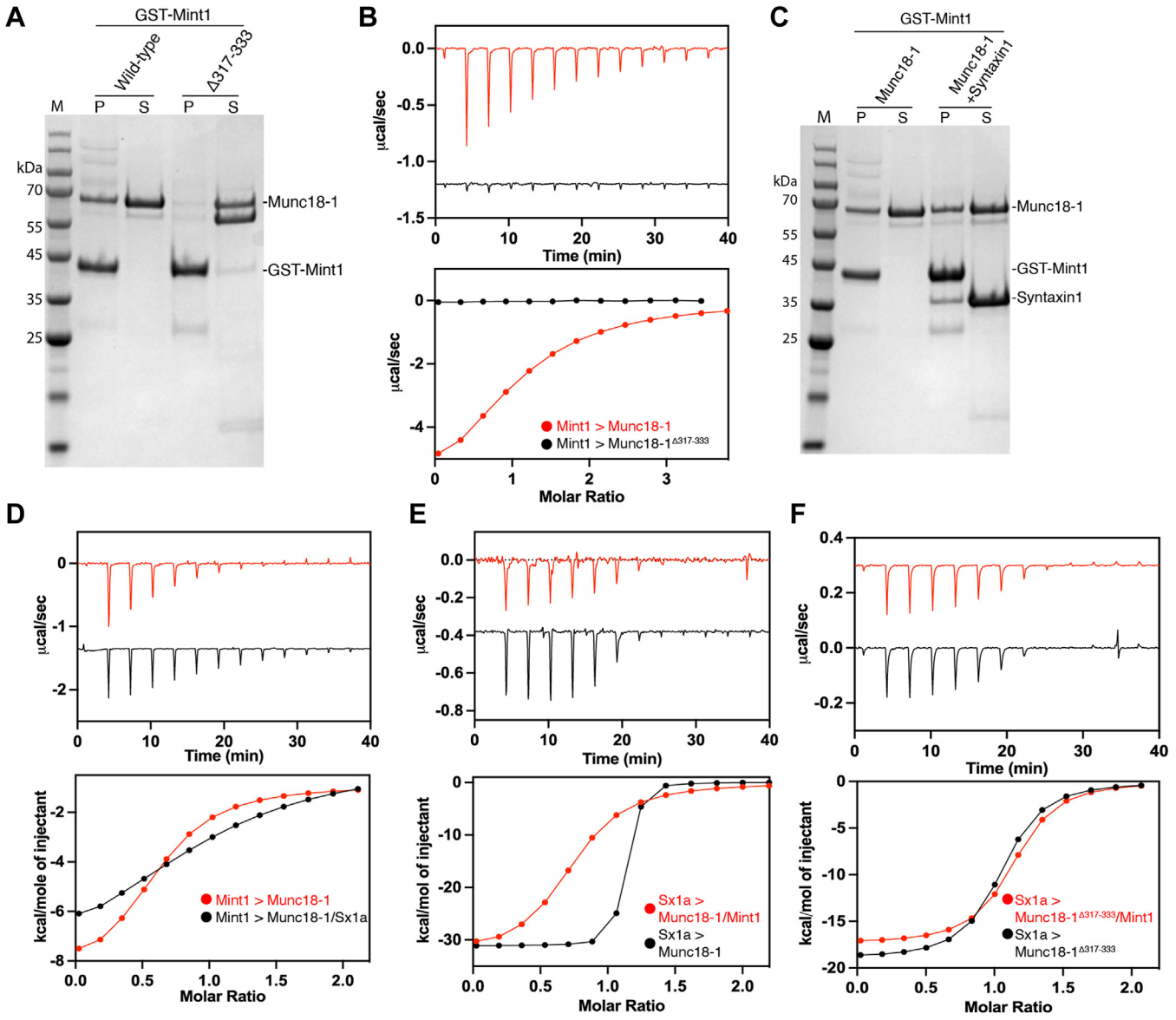

Figure 5. Mint1 and Sx1a show allosteric effects on binding to Munc18-1. *A*, pulldowns with GST-Mint1 MID show that Munc18-1 domain3a hinge loop is important for binding. As Mint1 does not contact domain3a, this suggests an allosteric effect on the domain3b-binding site. Image shows Coomassie-stained gel. *B*, ITC of synthetic Mint1$^{261–282}$ peptide binding to purified Munc18-1 (*red*) and Munc18-1$^{\Delta317–333}$ (*black*) confirms the requirement of domain3a for Mint1 interaction. *C*, pulldowns with GST-Mint1 MID show that Mint1 can bind Munc18-1 both alone and in the presence of Sx1a. Image shows Coomassie-stained gel. *D*, although Mint1 and Sx1a can bind Munc18 simultaneously, ITC of Mint1$^{261–282}$ AHM peptide binding to Munc18-1 in the absence (*red*) and presence (*black*) of Sx1a shows a reduction in binding affinity and enthalpy. *E*, ITC of Sx1a binding to Munc18-1 in the absence (*black*) and presence (*red*) of synthetic Mint1$^{261–282}$ peptide. Together, this shows there is a subtle allosteric inhibition of Sxa1 binding to Munc18-1 in the presence of Mint1. *F*, ITC of Sx1a binding to Munc18-1$^{\Delta317–333}$ in the absence (*black*) and presence (*red*) of synthetic Mint1$^{261–282}$ peptide. GST, glutathione-*S*-transferase; ITC, isothermal titration calorimetry; MID, Munc18-1-interacting domain; Mint, Munc18-interacting protein; Sx1a, Syntaxin1a.

practical indicator of a complex that was suitable for more detailed assessment. In these cases, we subsequently ran at least three modeling experiments focusing on the specific domains of Mint1 or Mint2 and the putative interactors that were predicted to interact with each other, to assess whether multiple predictions resulted in physically plausible structures that consistently aligned with each other in PyMOL (Tables S1 and S2).

Table 2
Thermodynamic parameters of Munc18-1 binding to Sx1a and Mint1 (261–282) by ITC

Syringe sample	Cell sample	K_d (μM)	N	ΔH (kcal/mol)	−TΔS (kcal/mol)	ΔG (kcal/mol)	Fold increase in K_d
Sx1a	Munc18-1	0.07 ± 0.2	1	−22.5 ± 2.4	11.4 ± 2.3	−11.1 ± 0	1
Sx1a + Mint1	Munc18-1 + Mint1	0.27 ± 0.5	1	−29.7 ± 1.9	20.7 ± 2.4	−9.0 ± 0.3	35
Mint1	Munc18-1	8.7 ± 0.2	1	−7.9 ± 0.01	0.9 ± 0.02	−6.9 ± 0.01	1
Mint1	Munc18-1 + Sx1a	20.6 ± 0.7	1	−8.9 ± 1.9	2.5 ± 1.7	−6.4 ± 0.1	2
Sx1a	Munc18-1$^{\Delta317–333}$	0.11	1	−18.6	9.1	−9.5	1
Sx1a + Mint1	Munc18-1$^{\Delta317–333}$ + Mint1	0.09	1	−18.8	9.2	−9.6	1

As expected, these *in silico* interaction screens with AlphaFold2 correctly predicted several well-characterized interactors, but they also provided validation of a number of prospective binding partners so far only identified in high-throughput screens (Figs. S6 and S7; Tables S1 and S2). Known interactors include the cytoplasmic NPxY motif of APP (12, 16, 18) and the CID sequence of CASK (26, 27), for which crystal structures have previously been determined. In addition, confident predictions were obtained for several other cytoplasmic sequences of transmembrane proteins previously identified to interact with Mint1 and/or Mint2 including lipoprotein receptors LRP1, LRP2, and LRP8 (20, 74), calsyntenin-1 (CSTN1) (75), and KCNJ12 (76). All these utilize variations of the NPxY motif found in APP to associate with the Mint PTB domains (Fig. 6). While LRP1, LRP2, and LRP8 each possess canonical NPxY sequences, CSTN1 and KCNJ12 are predicted to bind the same site of the PTB domain through divergent NPME and NELA sequences, respectively. One other protein identified in BioGRID was predicted with reasonable confidence to associate directly with Mint1. A putative complex between a C-terminal zinc-finger domain from the large protein WIZ (widely interspaced zinc finger–containing protein) was predicted to form with the tandem PDZ domains of Mint1 (Fig. S6 and Table S1).

We chose five predicted interactions to describe in more detail; (i) the association of the Mint1 and Mint2 PTB domains with a peptide sequence from the coiled-coil protein TJAP1 also called protein incorporated later into tight junctions (PILT) or tight junction protein 4 (TJP4) (Fig. 7), (ii) the association of the Mint1 and Mint2 tandem PDZ domains with ADP-ribosylation factor (ARF) GTPases ARF3 and ARF4 (Fig. 8*A*), (iii) the interactions of the C-terminal sequence of the neurexin-1 (NRX1) receptor with the PDZ2 domain of Mint1 or Mint2 (Fig. 8*B*), (iv) the interaction of an N-terminal YxxΦ motif in Mint1 with the μ3 subunit of the AP3 clathrin adaptor complex (Fig. 8*C*), and finally, the interaction of a Tyr-containing sequence in the N terminus of Mint2 with the neuronal ARF GTPase-activating proteins IQSEC1 and IQSEC2 (Fig. 8*D*).

Outside the canonical interactions of NPxY-related motifs with the Mint1 and Mint2 PTB domains, we were intrigued by a high-confidence prediction involving a short peptide sequence in TJAP1 (previously reported in high-throughput proteomic screens) (77) (Fig. S7 and Table S2). The TJAP1-binding site is distinct from the binding groove of NPxY motifs, and subsequent predictions of the Mint1 and Mint2 PTB domains in the presence of both the NPxY motif of APP and the peptide sequence from TJAP1 show highly consistent dual peptide interactions on opposite faces of the PTB domain (Fig. 7, *A* and *B*). Both the APP- and TJAP1-binding surfaces of Mint1 and Mint2 are highly conserved (Fig. 7*B*). The binding sequence of TJAP1 encompasses N-terminal residues ^{9}KPYRKAPPEHRELR^{22}, with buried aliphatic side chains and complementary electrostatic and hydrogen-bond contacts as shown in Figure 7*C*. The sequence ^{16}PEHR^{19} is predicted to form a β-turn structure where the Pro16 side chain forms a stacking interaction with the Arg19 guanidino group. To validate these AlphaFold2 predictions, we confirmed the binding of TJAP1 to Mint1 experimentally by ITC. Using the NPxY-containing sequence ^{750}SKMQQNGYENPTYKFFEQMQ^{769} of APP as a positive control, we confirmed that this bound to the Mint1 PTB domain with an affinity (K_d) of 0.3 μM (Fig. 7*D* and Table 3), similar to the affinity reported previously (12). The TJAP1 peptide ^{9}KPYRKAPPEHRELR^{22} bound to the Mint1 PTB domain with a modest affinity (K_d) of 20.9 μM (Fig. 7*E* and Table 3). Importantly, in competition experiments, the presence of the APP peptide did neither appreciably alter the TJAP1 affinity nor vice versa, confirming

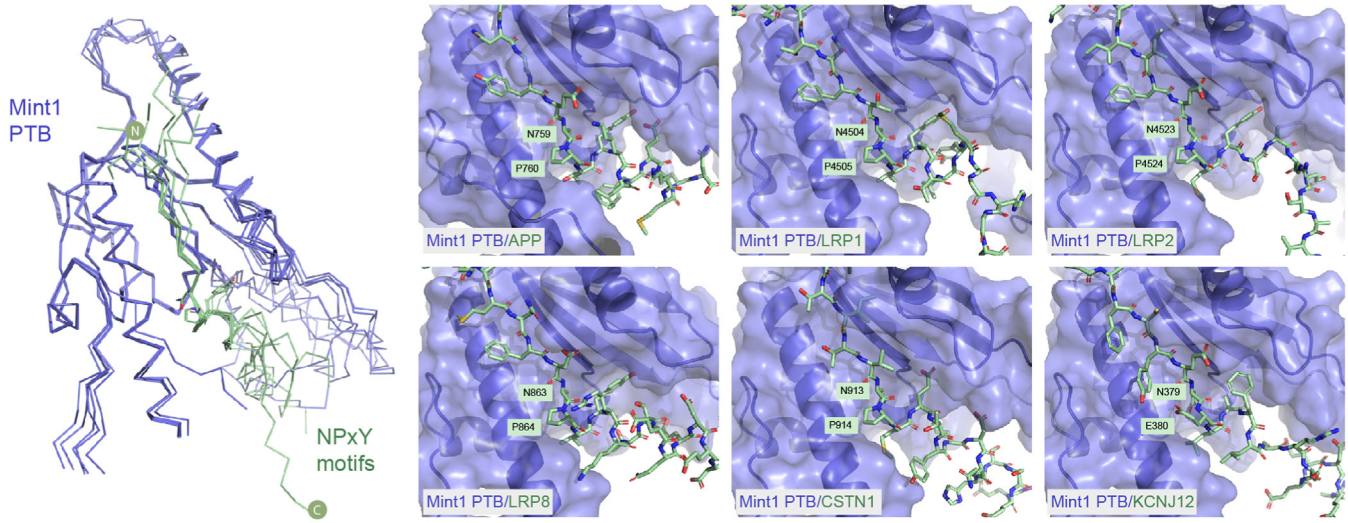

Figure 6. Interactions of the Mint PTB domains with canonical NPxY-containing peptide motifs predicted by AlphaFold2. Overlay of the top-ranked AlphaFold2-predicted structures of the Mint1 PTB domain (*blue*) in complex with various NPxY-related peptide motifs (*green*) shown in *backbone ribbon* representation. These sequences are predicted to bind the canonical binding groove of the PTB domain (with similar interactions predicted for Mint2 [not shown]). The *right panel* shows details of the different sequences derived from various Mint-interacting transmembrane proteins. Mint, Munc18-interacting protein; PTB, phosphotyrosine binding.

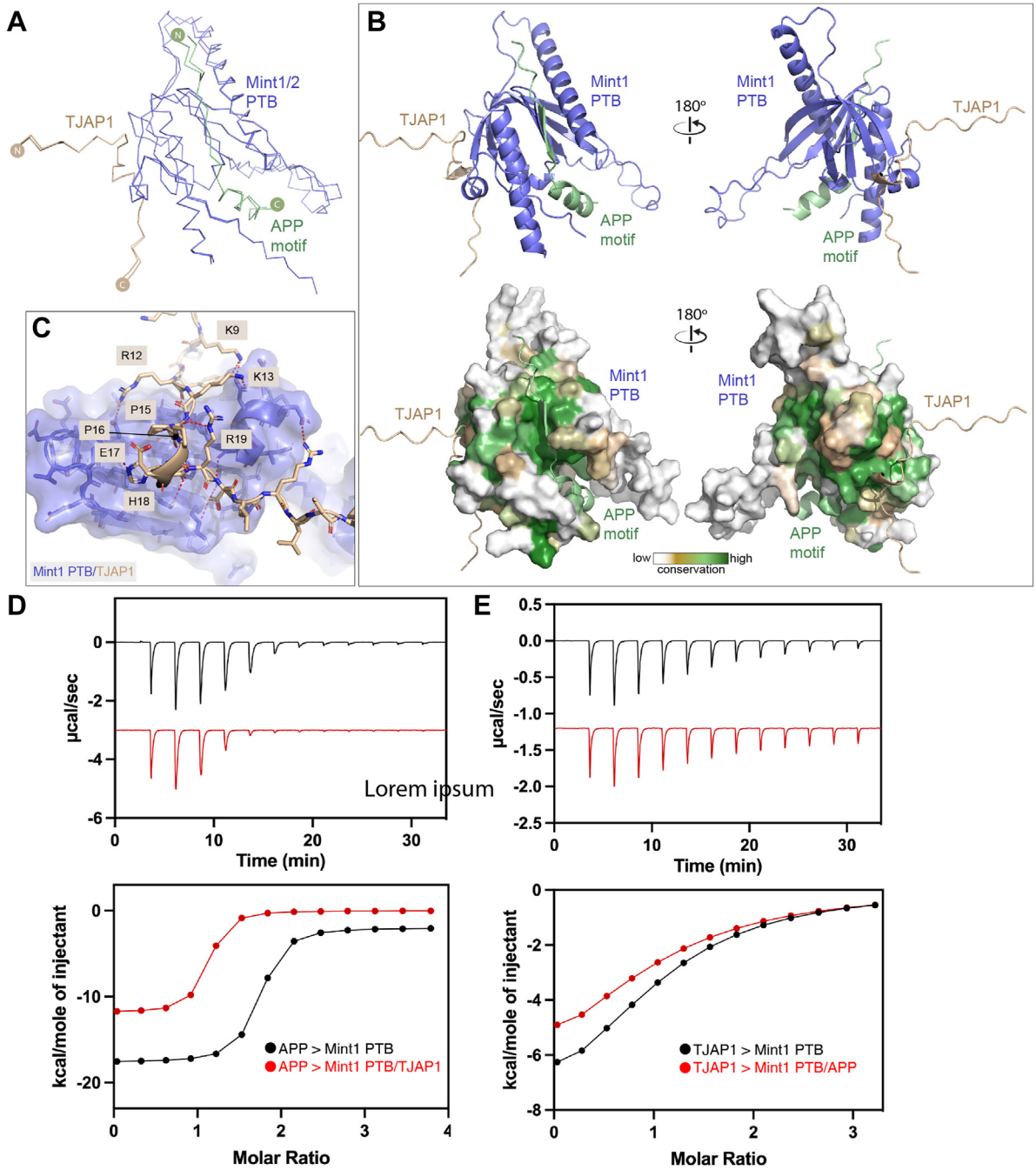

Figure 7. Interactions of the Mint PTB domains with a noncanonical peptide motif from TJAP1 predicted by AlphaFold2. *A*, overlay of the top-ranked AlphaFold2-predicted structures of the Mint1 and Mint2 PTB domains (*blue*) in complex with the APP NPxY motif (*green*) and the N-terminal peptide of TJAP1 (*brown*) shown in *backbone ribbon* representation. *B*, the top-ranked complex of Mint1 PTB domain bound to APP and TJAP1 is shown in *cartoon* representation. The *lower panel* shows the surface of Mint1 colored for sequence conservation as calculated by ConSurf (120). *C*, details of the Mint1 PTB domain interaction with the TJAP1 peptide. *D*, ITC of Mint1 PTB binding to the peptide motif from APP in the presence and absence of a peptide from TJAP1. *E*, ITC of Mint1 PTB binding to the peptide motif from TJAP1 in the presence and absence of a peptide from APP. The *top* shows raw ITC data, and the *bottom* shows integrated and normalized data fit to a 1:1 binding model. APP, amyloid precursor protein; ITC, isothermal titration calorimetry; Mint, Munc18-interacting protein; PTB, phosphotyrosine binding; TJAP1, tight junction–associated protein 1.

that the two peptides interact with distinct sites on Mint1 as predicted (Fig. 7, *D* and *E* and Table 3). These results show that the Mint PTB domains are capable of recruiting proteins *via* two distinct peptide motifs.

Mint2 was previously identified in a yeast two-hybrid screen for interactors of ARF3 (78). These screens identified fragments of Mint2 containing the tandem C-terminal PDZ domains, and subsequent experiments showed that Mint1, Mint2, and Mint3 could all interact with both ARF3 and ARF4. AlphaFold2 predictions of full-length Mint2 complexed with ARF3 and ARF4 revealed a very high-confidence interaction of the GTPases with the tandem PDZ domains,

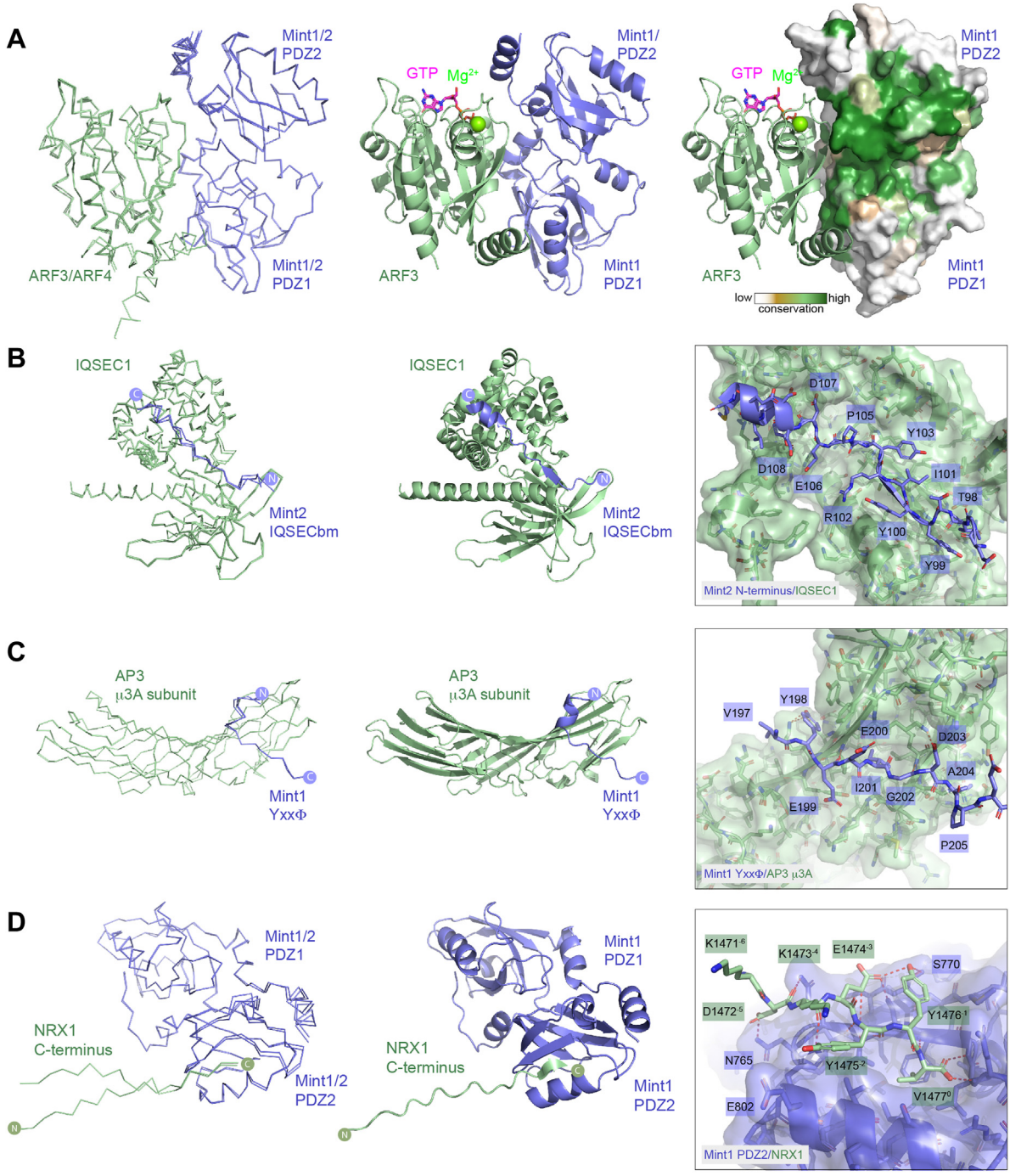

Figure 8. Interactions of the Mint N terminus and PDZ domains with novel binders predicted by AlphaFold2. *A*, overlay of the top-ranked AlphaFold2-predicted structures of the Mint1 and Mint2 tandem PDZ domains (*blue*) in complex with ARF3 and ARF4 (*green*) shown in *backbone ribbon* representation. The *middle panel* shows the Mint1 complex with ARF3 in *ribbon* representation, with the position of GTP and Mg^{2+} based on the previous crystal structure of active ARF3-GTP (79). The *right panel* shows the same image but with Mint1 surface colored for sequence conservation as calculated by ConSurf (120). *B*, overlay of the top-ranked AlphaFold2-predicted structures of the N-terminal Mint2 IQSEC binding motif (IQSECbm) (*blue*) in complex with the C-terminal Sec7 and PH domains of IQSEC1 (*green*) shown in *backbone ribbon* representation. The *middle panel* shows the top-ranked Mint2 complex with IQSEC1 in *ribbon* representation. The *right panel inset* shows the details of the Mint2 interaction with IQSEC1 PH domain. *C*, overlay of the top three-ranked AlphaFold2-predicted structures of the Mint1 YxxΦ motif (*blue*) in complex with the C-terminal μ-homology domain (MHD) of the AP3 μ3A subunit (*green*) shown in *backbone ribbon* representation. The *middle panel* shows the Mint1 complex with μ3A in *ribbon* representation. The *right panel inset* shows the details of the Mint1 YxxΦ motif interaction with μ3A. *D*, overlay of the top-ranked AlphaFold2-predicted structures of the Mint1 and Mint2 tandem PDZ domains (*blue*) in complex with the C-terminal PDZbm of NRX1 (*green*) shown in *backbone ribbon* representation. The *middle panel* shows the Mint1 complex with ARF3 in *ribbon* representation. The *right panel inset* shows the details of the NRX1 interaction with Mint1 PDZ2 domain. ARF, ADP-ribosylation factor; Mint, Munc18-interacting protein; NRX1, neurexin-1; PDZbm, PDZ binding motif.

Table 3
Thermodynamic parameters of Mint1 PTB domain binding to TJAP1 and APP peptides by ITC

Syringe sample	Cell sample	K_d (μM)	N	Δ*H* (kcal/mol)	−TΔ*S* (kcal/mol)	Δ*G* (kcal/mol)
TJAP1 (9–22)	Mint1 PTB	20.9 ± 2.4	1	−8.9 ± 0.9	2.5 ± 0.9	−6.4 ± 0.1
TJAP1 (9–22)	Mint1 PTB + APP (750–769)	29.4 ± 9.5	1	−7.1 ± 1.6	1.4 ± 1.8	−6.2 ± 0.2
APP (750–769)	Mint1 PTB	0.31 ± 0.01	1	−15.6 ± 0.7	6.7 ± 0.6	−8.9 ± 0.01
APP (750–769)	Mint1 PTB + TJAP1 (9–22)	0.58 ± 0.01	1	−11.8 ± 0.1	1.7 ± 1.1	−8.5 ± 0.01

correlating with the yeast two-hybrid studies (78) (Fig. S7 and Table S2). Predictions focused on the Mint1 and Mint2 PDZ domains subsequently produced highly consistent complex structures with the two GTPases (Fig. 8*A*). The structure of activated ARF3-GTP bound to a bacterial toxin called MARTX was previously solved by X-ray crystallography (79). AlphaFold2 predicts ARF3 and ARF4 to be in the active GTP-Mg^{2+}-loaded conformation when bound to Mint1 and like the bacterial effector Mint1 and Mint2 primarily engage the switch 2 and interswitch regions of the GTPases, making little contact with the switch 1 region. The ARF GTPases bind an extensive and conserved surface with the interface composed of regions from both PDZ1 and PDZ2 domains in the tandem PDZ structure.

As well as the ARF GTPases, two neuronal ARF GTPase-activating proteins IQSEC1 and IQSEC2 (IQ motif and SEC7 domain–containing proteins), were also predicted to bind to an N-terminal sequence in Mint2 ^{96}GITYYIRYCPEDD^{108} (Figs. 8*B* and S1). The core binding sequence consists of several Tyr side chains from Mint2 that stack along a conserved surface groove in the C-terminal PH domain of IQSEC1 and IQSEC2, with complementary electrostatic contacts also made by downstream Glu and Asp residues from Mint2 with Lys and Arg side chains in IQSEC proteins. Although the sequence is semiconserved in Mint1 homologs (Fig. S1), AlphaFold2 does not predict a confident interaction with these proteins (not shown), suggesting their sequences are less optimized for binding. The IQSEC1 and IQSEC2 proteins are Ca^{+}/CaM-regulated synaptic proteins that can activate all members of the ARF GTPase family (80-82) and are mutated in neuronal developmental disorders including X-linked intellectual disability with early onset epileptic encephalopathy (83, 84). Notably, the IQSEC1 protein was previously shown to bind a short Tyr-containing sequence in the C terminus of the GluA2 α-amino-3-hydroxyl-5-methyl-4-isoxazole-propionate receptor *via* the PH domain (85), and we speculate that Mint2 and GluA2 may utilize the same binding site in the IQSEC proteins.

The next predicted interaction we examined in detail was that of Mint1 with the μ3 subunit of the tetrameric AP3 clathrin adaptor complex (Fig. 8*C*), another unexpected association reported in the same high-throughput screens as TJAP1 (77). The μ3 subunit has an N-terminal longin domain that embeds it within the AP3 tetramer, and a C-terminal μ-homology domain that associates with YxxΦ tyrosine-based motifs (where Φ is a bulky hydrophobic residue), typically in transmembrane cargos for sorting from endosomes to lysosomal compartments (86, 87). The predicted structure of the Mint1 ^{298}YEEI^{301} sequence closely resembles the crystal structure of the TGN38 motif YQRL bound to the rat μ3 μ-homology domain, with both Tyr298 and Ile301 inserting into complementary surface pockets as typically seen for YxxΦ motifs. We also tested AlphaFold2 predictions of the Mint1 sequence with other μ-subunits from AP1, AP2, AP4, and AP5. While μ1, μ2, and μ4 proteins were each predicted to form a complex, the iPTM confidence scores were much lower than μ3, and μ5 was not predicted to bind at all.

Although not listed in the BioGRID entries for Mint1 or Mint2, other studies proposed that their PDZ domains interact with C-terminal sequences of NMDA receptors, kalirin-7, NRX1, ApoER2/LRP8, and LDLR (19-23). PDZ domains are small scaffolds that bind to PDZbms typically found at the C terminus of their interacting proteins. They fall into three main classes; type 1 with consensus [S/T]xΦ (x = any amino acid; Φ = hydrophobic amino acid), type 2 with consensus ΦxΦ, and type 3 with consensus [E/D]xΦ (88, 89). We used AlphaFold2 to predict the interaction of the Mint1 and Mint2 PDZ domains with the C-terminal sequence of NRX1, which conforms to type 2 PDZbm. This confidently predicted an interaction between the C-terminal ^{1471}KDKEYYV^{1477} NRX1 sequence with the second PDZ2 domain of the PDZ1–PDZ2 tandem structure (Fig. 8*D*). The C-terminal Val1477 side chain (position "0" in standard PDZbm nomenclature) docks in a complementary hydrophobic pocket with the terminal carboxyl group hydrogen bonding with the backbone amides of Mint1 Leu759 and Gly760. The NRX1 Tyr1475 and Tyr1476 side chains at positions −1 and −2 pack into complementary surface grooves, whereas both main-chain and side-hydrogen bonds upstream of the C-terminal interaction provide further specificity. This requires experimental validation, but combined with the fact that the C-terminal Mint1 sequence PVYI (PLIY in Mint2) itself can form an intramolecular *cis*-interaction with its own PDZ1 domain (90), it suggests that the PDZ2 domain of the Mint proteins provides the major platform for recruiting PDZbm-containing *trans*-ligands.

While we have focused on proteins that *are* predicted to bind to Mint1 or Mint2, it is notable that from the list of putative BioGRID interactors, the majority are *not* predicted to associate directly with the Mint adaptors, including many that have previously been identified using methods such as co-IPs (Tables S1 and S2). In some case, this could be due to limitations with the predictive ability of AlphaFold2 or potentially other requirements such as PTMs not accurately represented in AlphaFold2 predictions. However, we propose that many of the proteins reported in BioGRID either bind indirectly (*via* other proteins not included in our binary predictions) or are nonspecific interactions detected by the proteomics methods.

Discussion

The interaction of Mint proteins with Munc18-1 has long been known to be important for synaptic neurotransmitter and hormonal release through the regulation of SNARE-mediated vesicle fusion. While the molecular basis for the scaffolding and trafficking of the APP transmembrane protein and CASK adaptor has been structurally characterized (12, 16, 18, 26, 27), until recently, the mechanism by which Mints bind to Munc18-1 was unknown. In this work, and in a recent study by Li *et al.* (47), the interaction is revealed to be *via* the binding of Munc18-1 domain3b to a conserved AHM in the N-terminal unstructured domains of the Mint1 and Mint2 neuronal homologs. The binding surface on Munc18-1 is distinct from its known binding sites for the Sx1a and VAMP2 SNARE proteins, although we find there is a small but significant reduction in the binding affinity of Sx1a in the presence of the Mint1 AHM. In line with a role for the Mint1 interaction in Munc18-1-dependent exocytosis, we observed that perturbation of Munc18-1 Mint-1 interaction in domain 3b impacted exocytosis in neurosecretory cells. We speculate this could point to a role of Mint proteins in regulating the SNARE complex dynamic templating activity of Munc18-1, which will be worth future investigation.

The AHM sequence found in Mint1 and Mint2 is conserved across many species, although it appears not to be present in some organisms such as nematodes and flies. Furthermore, it may be relatively specific to the Mint proteins, with few if any other proteins possessing similar motifs. We scanned the human genome using ScanProsite and did not find any other proteins with highly similar sequences. Li *et al.* (47) reported potential AHMs in Munc13-1, Bassoon, and Atg16L, although no binding was detected using the putative motif from Munc13-1 by ITC. Future proteomic studies of Munc18-1 using specific domain3b mutations may confirm the existence of other proteins able to bind this site, but there are unlikely to be a large number. Like the CASK-binding CID sequence in Mint1, the Mint1 and Mint2 AHM sequences lie within their extended and intrinsically unstructured N-terminal domain, likely adopting their α-helical structures *via* induced folding upon Munc18-1 interaction. This may explain the relatively modest binding affinity for Munc18-1 despite the reasonably large binding surface. The interaction between these proteins is thus likely highly context dependent, relying on both their specific coupling as well as their colocalization at the membrane surface and likely clustering with other proteins, such as the SNAREs, APP, neurexins, and potentially small GTPases like ARF3.

In addition to dissecting the mechanism of Mint1 and Mint2 interaction with Munc18-1, we have used machine learning–based structure prediction with AlphaFold2 to assess the broader interactome of the Mint proteins. These predictions provide insights into those interactions that are likely to be *directly* mediated by the Mint proteins, as validated in one instance with the direct binding of TJAP1 confirmed. Our results thus provide an example of how AlphaFold2 and similar algorithms can be used as a type of triage of large proteomic datasets, providing additional confidence in the plausibility of direct interactions (73, 91-95). Such an approach has the potential to inform and accelerate subsequent experimental validation of molecular complexes detected in high-throughput screens, by providing greater assurance as to which hits represent specific interactors.

Apart from the expected predictions of CASK and APP, for which previous crystal structures are available, there were several other notable complexes that were confidently modeled by AlphaFold2 in this study. A number of proteins have been reported to interact with the PDZ domains of Mint1 and Mint2 *via* C-terminal PDZbms, including calcium channels (96), kalirin-7 (21, 97), NMDA receptors (23), and NRX1 (19, 98). Furthermore, the C terminus of Mint proteins can form an intramolecular interaction with their own PDZ1 domain, acting as an autoinhibitory sequence of PDZ1 (90). Taking NRX1 as an example, we found that its type II PDZbm was strongly predicted to interact with the PDZ2 domain in the canonical β-strand orientation, and since other neurexin homologs share the same C-terminal sequence, they likely use the same binding mechanism. This hypothesis, as well as whether the second PDZ2 domain is bound by other PDZbms, warrants further experimental studies.

One novel Mint interactor predicted by AlphaFold2 and validated in direct binding experiments was TJAP1, which was previously identified in high-throughput proteomic screens with all three Mint homologs (77). TJAP1 has an N-terminal unstructured region, which we predicted to interact with Mint PTB domains, a central-coil region predicted by AlphaFold2 to form a homodimer (not shown), and an extended C-terminal unstructured and proline-rich domain. The precise function of TJAP1 is essentially unknown, although it was identified in yeast two-hybrid assays to bind the GTPase ARF6 (99) and discs large-2 (Dlg-2/PSD93) (100), a member of the membrane-associated guanylate kinase protein family that includes CASK (101). TJAP1 is localized to both the Golgi and tight junctions (100, 99), and the putative interaction with the TJAP1 N-terminal peptide sequence is confidently predicted with not only the neuronal Mint1 and Mint2 proteins but also the ubiquitous Mint3 protein (not shown), so it is probable that the association is important in diverse cell types as well as in neurons.

The ARF3 and ARF4 small GTPases were originally identified to bind Mint proteins in yeast two-hybrid screens (78); however, no subsequent studies have examined the mechanism or functional role of these interactions. Our modeling indicates a conserved binding site involving the PDZ1 and PDZ2 tandem domains of the Mint proteins, which supports the original yeast two-hybrid mapping experiments (78). ARF3 is highly enriched in the brain, and both proteins play a role in maintaining recycling endosome morphology and integrity (102, 103). Interestingly, ARF3 mutations have recently been found in patients with neurodevelopmental disorders characterized by brain abnormalities, microcephaly, and seizures (104, 105). It is tempting to speculate that these disorders may overlap with synaptic pathologies caused by mutations in Munc18-1, CASK, and other synaptic proteins, thus suggesting

a role for ARF3 in the synaptic vesicle trafficking pathways that could in part be mediated through the Mint proteins.

The last predicted interaction we examined was that of Mint1 with the AP3 clathrin adaptor complex. This involves binding of the AP3 μ3A domain with a canonical YxxΦ sequence in the Mint1 N-terminal region (not present in Mint2 or Mint3). This would indicate that the Mint1 N terminus has at least two functions distinct from the other Mint isoforms; the ability to bind CASK and the potential to couple Mint1 and bound proteins (such as, *e.g.*, APP or neurexins) into AP3-mediated transport structures. AP3 is primarily found on endosomes, where it mediates trafficking to lysosomes and lysosome-related organelles (87), and depending on specific subunit isoforms, it has important roles in axonal transport and synaptic function by regulating the reformation of synaptic vesicles from endosomes derived from bulk synaptic endocytosis (106-112). Similar to ARF3, mutations in neuronal AP3 isoforms can lead to neurodevelopmental disorders with some overlapping features with other synaptopathies (38), suggesting a potential functional overlap of Mint1 and AP3 in synaptic integrity (113, 114).

An overall model for Mint1 is shown in Figure 9 summarizing the known and predicted interactions mediated by this scaffold protein. Figure 9*A* shows an AlphaFold2 prediction of the full-length protein highlighting binding sequences and structural domains of the protein and underlines the highly extended nature of the N-terminal intrinsically disordered domain containing the Munc18-1 binding AHM as well as

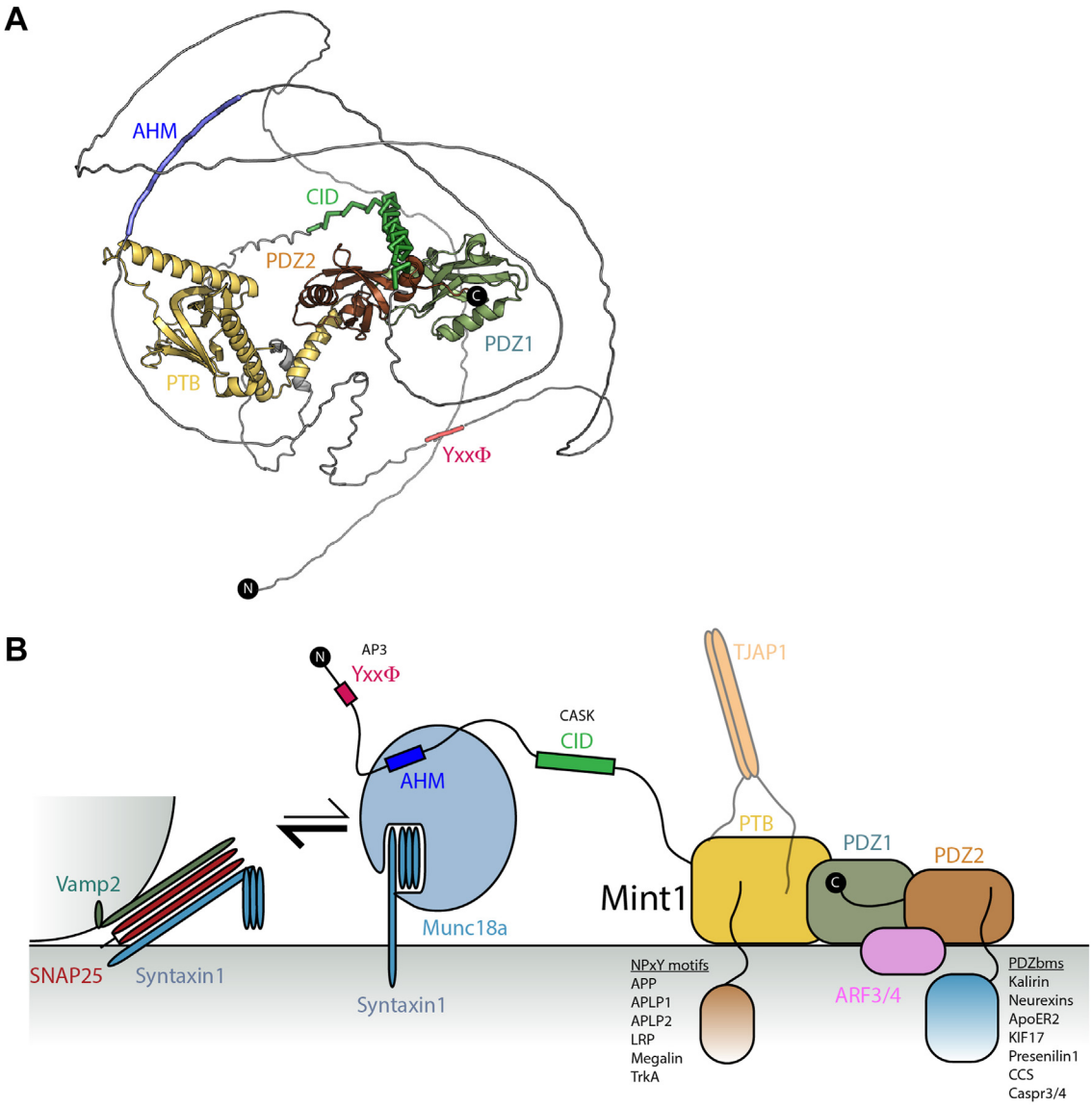

Figure 9. Mint1 structural model and interactions. *A*, structural model of Mint1 derived from AlphaFold2 (113). *B*, schematic summary of Mint1-mediated interactions, and speculative model suggesting that at the cell surface, Mint1 may act to reduce the affinity of Munc18-1 for the autoinhibited Sx1a, thus enhancing the ability of Sx1a to associate with VAMP2 and SNAP25 to form the *trans*-SNARE assembly required for vesicle fusion. The C-terminal domains of Mint1 in contrast are associated with other proteins containing NPxY and PDZbm sequences and ARF small GTPases that may enhance Mint1 membrane recruitment and modulate transmembrane protein trafficking. ARF, ADP-ribosylation factor; Mint, Munc18-interacting protein; PDZbm, PDZ binding motif; Sx1a, Syntaxin1a.

binding motifs for the AP3 adaptor and CASK. Figure 9*B* is a cartoon summary of the interactions described previously and highlights the overall scaffolding function of this protein. From our biophysical and biochemical studies, we speculate that the reduced affinity of Sx1a for Munc18-1 in the presence of the Mint AHM sequence could lead to an enhancement of SNARE assembly mediated by Munc18-1 templating, although this will require more extensive testing. A final caveat to this model is that it does not account for temporal regulation of the various interactions, the impact of PTMs, or the cellular environment where each interaction is likely to occur including the plasma membrane and other organelles such as endosomes and the Golgi.

In summary, we have mapped and characterized the specific association of the neuronal Mint1 and Mint2 proteins with the SNARE regulatory protein Munc18-1 providing a high-resolution snapshot for how these key synaptic proteins interact with other, confirming and extending recent related work (47). This study further emphasizes the ability of AlphaFold2, at least in many instances, to predict protein–peptide interactions with a high degree of accuracy. By applying a wider set of systematic analyses, our work has revealed likely modes of interaction between the Mint proteins and a variety of known and novel effectors, which provides a foundation for future mechanistic studies of their important role in synaptic activity.

Experimental procedures

All resources and reagents are listed in Table S3.

Antibodies, plasmids, and peptides

Human Mint1 sequences for bacterial expression were codon optimized and subcloned into the pGEX4T-2 plasmid by Genscript. The constructs generated were GST-tagged Mint1 (226–314) (MID), Mint1 (261–272), Mint1 (261–282), Mint1 (226–289), Mint1 (222–314), and Mint1 (237–289). Human Mint1 open reading frame and mutant Mint1 (D269A/I270A) were obtained from Genscript and cloned into the pcDNA3.1-N-eGFP. The human Mint1 PTB domain (residues 448–623) sequence was synthesized and cloned into pGEX6P-2 by Gene Universal.

All Mint-derived synthetic peptides were purchased from Genscript. The human APP (750–769) (SKMQQNGYENPTYKFFEQMQ) and TJAP1 (9–22) (KPYRKAPPEHRELR) peptides were made by solid phase peptide synthesis in-house, purified by reverse-phase HPLC, and purity assessed by mass spectrometry. GFP polyclonal antibody and goat antimouse secondary antibody were purchased from Thermo Fisher, and mouse monoclonal anti-Munc18-1 was purchased from BD Biosciences. pmEos3.2-N1 Munc18-1^{WT} was created by restriction digestion of Munc18-1^{WT} (double digestion with NheI–AgeI, New England Biosciences) from pmEos2-N1 Munc18-1^{WT} (65), and vector linearization of pmEos3.2-N1 with NheI–AgeI was followed by T4 ligation. pmEos3.2-N1 Munc18-1^{WT} was then used as a template to introduce the following missense mutation R388A using QuickChange Lightning site-directed mutagenesis kit (Agilent Technologies, catalog no.: 210518) as per the manufacturer's instructions. Primers were designed by PrimerX (site: http://bioinformatics.org/primerx/) and ordered from Sigma–Aldrich. M18-1_R388A_For: 5′-GAAAAAATCAAGGACCCCATGGCAGCCATTGTCCCCATCCTGC-3′ and M18-1_R388A_Rev: 5′-GCAGGATGGGGACAATGGCTGCCATGGGGTCCTTGATTTTTTC-3′. All new plasmids were verified by Sanger sequencing performed by the Australian Genome Resource Facility. pCI VAMP2-pHluorin was a kind gift from James Rothman (115).

Recombinant protein expression and purification

All proteins were expressed in *Escherichia coli* Rosetta BL21 (DE3) cells. GST-Mint1 (226–314, the MID), containing pGEX4T-2 vector was transformed into Rosetta cells and plated on an LB/agar plate supplemented with ampicillin (0.1 mg/ml). Single colony was then used to inoculate 50 ml of LB medium containing ampicillin (0.1 mg/ml). And the culture was grown overnight at 37 °C with shaking at 180 rpm. The following day, 1 l of LB medium containing antibiotics ampicillin (0.1 mg/ml) and chloramphenicol (0.034 mg/ml) was inoculated using 10 ml of the overnight culture. Cells were then grown at 37 °C with shaking at 180 rpm to an absorbance of 0.7 to 0.8 at 600 nm, and the protein expression was induced by adding 0.5 mM IPTG. Expression cultures were incubated at 20 °C overnight. And the cells were harvested next day by centrifugation at 4000 rpm for 15 min using Beckman rotor JLA 8.100. Cell pellets were resuspended in 20 ml (for cell pellet from 1 l) of lysis buffer (50 mM Tris, pH 8.0, 500 mM NaCl, 10% glycerol, 1 mM DTT, benzamidine [0.1 mg/ml], and DNAse [0.1 mg/ml]). Resuspended cells were further lysed by using the cell disrupter (TS-Series; Constant Systems, LTD), and the soluble fraction containing GST-Mint1 was separated from cell debris by centrifugation at 18,000 rpm for 30 min at 4 °C. The soluble fraction was first purified by affinity chromatography using glutathione-Sepharose resin, and the GST-Mint1 was eluted using 50 mM Tris, pH 8.0, 500 mM NaCl, 10% glycerol, 1 mM DTT buffer, and the protein containing fractions were concentrated and further purified by gel filtration chromatography (Superdex 75 [16/600], GE Healthcare). GST-Mint1-containing fractions were analyzed by SDS-PAGE. All the other GST-Mint1 N-terminal constructs (GST-Mint1 261–272, 261–282, 226–289, 222–314, and 237–289) were also expressed and purified as described previously. The GST-Mint1 PTB domain was expressed as aforementioned, but the GST tag was removed by incubation with Prescission protease, followed by gel filtration into 50 mM Hepes, 200 mM NaCl, 0.5 mM Tris(2-carboxyethyl)phosphine (TCEP), and 5% glycerol.

For GFP-nanotrap preparation, the plasmid pOPINE harboring His-SUMO-GFP-nanotrap was transformed into *E. coli* Bl21 (DE3) cells and plated on an LB/agar plate supplemented with ampicillin. GFP-nanotrap refers to the camelid-derived nanobody specific for GFP (116). The expression and lysis of cells were carried out as described

previously. The supernatant containing GFP-nanotrap was first purified by affinity chromatography using Talon resin equilibrated with 50 mM Tris (pH 8.0), 500 mM NaCl, 10% glycerol, and protein bound to the column was eluted using elution buffer containing 50 mM Tris (pH 8.0), 500 mM NaCl, 10% glycerol, and 300 mM imidazole. The fractions containing GFP-nanotrap were combined, concentrated, and loaded on to a Superdex 75 (16/60) column equilibrated with 50 mM Hepes (pH 7.5), 200 mM NaCl, and 0.5 mM TCEP. The fractions containing the protein were analyzed by SDS-PAGE, combined, and concentrated to the desired concentration. Rat Sx1a ($Sx1_{1-261}$-His), Munc18-1-His, and Munc18-$1^{\Delta 317-333}$ were also expressed and purified to homogeneity as described by Hu *et al.* (71).

Cell culture and transfection

Neurosecretory cell line, pheochromocytoma cells (PC12), and Munc18-1/2 DKO PC12 cells (DKO-PC12) (60) were cultured at 37 °C/5% CO_2 in normal culture media (Dulbecco's modified Eagle's medium [high glucose, pyruvate, Gibco, catalog no.: 11995], 7.2% heat-inactivated fetal bovine serum [Gibco], 7.2% heat-inactivated horse serum [Gibco], 1× GlutaMAX supplement [Gibco, catalog no.: 35050061]). Cells were transfected using Lipofectamine LTX (Invitrogen, catalog no.: 15338100) as per the manufacturer's instructions. For co-IP experiments, 4×10^6 of PC12 cells were cultured in 10 cm culture dishes (TPP Techno Plastic Products AG) coated with 0.1 mg/ml poly-D-lysine (Sigma; catalog no.: P2636). For each condition 15.3 μg plasmid DNA was used per 10 cm dish, and 2 × 10 cm dishes were pooled for experiments. PC12 cells were transfected with either pEGFP-N1 (GFP control), pcDNA3.1-N-eGFP hMint1 WT, or pcDNA3.1-N-eGFP hMint1 DI/AA mutant, and 48 h post-transfected cell pellets were collected for subsequent co-IP/GFP Trap.

Munc18 DKO-PC12 cells were cotransfected with 1 μg pCI VAMP2-pHluorin and 1 μg of either pmEos3.2-N1 Munc18-1WT or pmEos3.2-N1 Munc18-1 R388A with 6.75 μl Lipofectamine LTX with PLUS Reagent (ThermoFisher, catalog no.: 15338-100) into 3.5 cm petri dishes as per the manufacturer's instructions. Cells were replated after 24 h onto 0.1 mg/ml poly-D-lysine (catalog no.: P2636-100MG)–coated glass-bottom petridishes (Cellvis, catalog no.: D29-20-1.5-N) and imaged 48 h after transfection.

Co-IP

PC12 cells containing EGFP, GFP-hMint1 (WT), GFP hMint1 DI/AA were lysed on ice using buffer composed of 20 mM Hepes, 50 mM NaCl, 1% Triton, 1 mM DTT, DNAse, and a tablet of protease inhibitor cocktail. To further enhance the lysis, the lysate was aspirated through a small needle approximately ten times. The lysate was then centrifuged at 17,000*g* for 15 min to separate the cellular debris from the supernatant containing the soluble proteins. About 50 μl of GFP-nanotrap coupled to NHS-activated Sepharose 4 beads were added to each of the three supernatants containing GFP, GFP-hMint1 WT, and GFP-hMint1 DI/AA. The supernatant–bead mixtures were incubated for 2 h at 4 °C while shaking, and then the beads were spun down by at 5000*g* for 2 min to remove the unbound proteins. The bead samples were washed three times using the lysis buffer, and 50 μl of SDS sample buffer was added to each sample. The beads, containing the immunoprecipitated proteins, were boiled at 95 °C for 5 min to elute the bound proteins and resolved using Western immunoblotting. GFP and Munc18a proteins were detected using anti-GFP mouse and anti-Munc18a mouse as primary antibodies, respectively, and goat antimouse antibody as the secondary antibody. The final imaging was performed using ECL and Odyssey infrared imaging system (LI-COR).

TIRF microscopy and cell footprint analysis

For live-cell TIRF imaging, transfected Munc18 DKO-PC12 cells were imaged in glass-bottom dishes bathed in buffer A (145 mM NaCl, 5 mM KCl, 1.2 mM Na_2HPO_4, 10 mM D-glucose, 20 mM Hepes, pH 7.4) and imaged immediately before and following 2 mM $BaCl_2$ stimulation to elicit vesicle fusion (117). Dishes were imaged on an iLas2 Microscope (Roper Scientific) equipped with a Nikon CFI Apo TIRF 100×/1.49 numerical aperture oil-immersion objective and an Evolve 512 Delta EMCCD camera (Photometrics) and Metamorph Imaging Software, version 7.7.8. Cells were imaged at 10 Hz (100 ms acquisition), for 3000 frames (300 s) at 37 °C/5% CO_2, and 30% of the initial 491 laser power in TIRF.

Vesicle fusion assays in Munc18 DKO cells

To assess vesicle fluorescence over time, a custom Python 3.8 pipeline was developed. For a typical 3000 frame TIRF acquisition, the data were read into a Python z-stack and divided into 100 frame intervals. The fluorescence at each interval was averaged, and fluorescent puncta identified at pixel resolution (where one pixel = 106 nm) using the Laplacian of Gaussian functionality of Python OpenCV. The puncta were used to populate a 3D [x,y,t] array. 3D DBSCAN (scikit-learn) was used to identify clusters of puncta, which were within one pixel spatially and two pixels temporally. The time corresponding to the disappearance of each cluster was used as the indicator of a completed fusion event. Ongoing clusters that had not disappeared by the end of the acquisition were not considered for further analysis.

Statistical analysis of vesicle fusion events in Munc18 DKO cells

Unless otherwise stated, values are represented as mean ± SEM. The tests used for statistical analysis are indicated in the respective figure legends. Nonparametric Mann–Whitney *U* test was used to compare two groups of for non-normally distributed data. Comparisons of the same cells analyzed before and after stimulation were analyzed by a paired statistical test. Data were considered significant at $p < 0.05$.

ITC

For ITC, all peptides were weighed and initially dissolved in the working buffer to make a stock concentration of 2 mM. ITC experiments measuring Munc18-1 binding to Mint1 peptides and Sx1a were carried out on Microcal iTC200 at 25 °C. GST-Mint1 and all the other proteins used in the experiments were buffer exchanged into 50 mM Tris (pH 8.0) and 200 mM NaCl by gel filtration prior to ITC. GST-Mint1 (1 mM), Sx1a (1 mM), or Mint1 synthetic peptide (0.7 mM) were titrated into Munc18-1-His (50 μM). Mint1 PTB domain binding to the APP and TJAP1 peptides was performed in 50 mM Hepes, 200 mM NaCl, 0.5 mM TCEP, and 5% glycerol at 25 °C with 1 mM peptides titrated into 50 μM Mint1 PTB domain. The binding parameters, equilibrium constant K_a ($1/K_d$), stoichiometry (n), and the enthalpy (ΔH) were determined by processing the ITC data using ORIGIN 7.0 software. The equation, $\Delta G = \Delta H - T\Delta S$, was used to calculate the Gibbs free energy (ΔG), and all the experiments were performed in triplicate or duplicate to calculate the SEM for thermodynamic parameters.

Pull-down assays

Pull-down assays were carried out using GST-Mint1 and Munc18-1-His. About 0.5 nmol of GST-Mint1 was mixed with 1 nmol of Munc18-1-His in 500 μl of pull-down buffer (50 mM Tris [pH 8.0], 200 mM NaCl, 1 mM DTT, and 0.1% IGEPAL) and incubated for 30 min on a rotating holder at 4 °C. The protein mixture was then centrifuged at full speed for 5 min, and 50 μl of glutathione Sepharose resin pre-equilibrated in pull-down buffer was added. The protein mix with the resin was incubated further 30 min at 4 °C on a rotating holder, and at the end of the incubation, the beads were spun down at 5000 rpm for 30 s. The supernatant containing the unbound protein is pipetted off, and the beads with the bound protein were washed four times with 1 ml of pull-down buffer. About 50 μl of SDS sample buffer was added to the beads and analyzed by SDS-PAGE for bound proteins.

Protein structural prediction, modeling, and visualization

All protein models were generated using AlphaFold2 Multimer (53, 54) implemented in the ColabFold interface available on the Google Colab platform (59). For each modeling experiment, ColabFold was executed using default settings where multiple sequence alignments were generated with MMseqs2 (118). For all final models displayed in this article, structural relaxation of peptide geometry was performed with AMBER (119). For all modeling experiments, we assessed (i) the prediction confidence measures (pLDDT and interfacial iPTM scores), (ii) the plots of the PAE, and (iii) backbone alignments of the final structures. For modeling of the complex between Munc18-1 and Mint1, we initially predicted the complex between full-length proteins and identified a high-confidence binding sequence in the N-terminal region of Mint1 that correlated precisely with the binding motif identified in our biochemical experiments. Based on this initial model and our biochemical mapping of the minimal Mint1 sequence for Munc18-1 binding, we performed multiple independent predictions using a shorter peptide region, combined with AMBER energy minimization to optimize amino acid stereochemistry.

For interactome-wide analysis of other protein–protein interactors of Mint1 and Mint2, we obtained a list of putative interactors from the BioGRID repository (72) and predicted whether they formed direct complexes using the ColabFold Batch implementation of AlphaFold2 (59) (Tables S1 and S2). To assign a direct "interactor" from these *in silico* analyses, we used an approach similar to recent work by Sifri *et al.* (73). We initially assessed both the AlphaFold2-derived iPTM score and the resultant PAE graphs, which provide confidence metrics for the interactions between the proteins. For those with promising scores, we also examined the predicted structures in PyMOL to assess whether interacting regions involved the expected complementary hydrophobic, polar, and electrostatic contacts. To conserve GPU resource allocation, we initially generated three separate predictions of each putative complex in AlphaFold2 in unsupervised batch mode. We found that a minimum average iPTM score of ∼0.3 combined with a strong signal in the PAE plots for intermolecular structural correlation typically provided a useful indicator of a complex that was suitable for further assessment. In these cases, we subsequently ran at least three modeling experiments focusing on the specific domains of Mint1–Mint2 and the putative interactors that were predicted to interact with each other to assess whether multiple predictions resulted in physically plausible structures that consistently aligned with each other in PyMOL (Tables S1 and S2). Sequence conservation across Protein Data Bank models was mapped with ConSurf (120). All structural images were made with PyMOL (Schrodinger; https://pymol.org/2/).

Data availability

All data are contained within the article.

Supporting information—This article contains supporting information.

Acknowledgments—We thank Lionel Louiset, Ailisa Blum, Pranesh Padmanabhan, and Jenny Martin for the assistance with this work, including initial mammalian construct testing, funding contributions, and supervision of students.

Author contributions—R. S. G., T. P. W., F. A. M., and B. M. C. methodology; S. W., E. K. L., T. P. W., and A. J. formal analysis; S. W., R. S. G., A. M., A. T. B., and B. M. C. investigation; S. W., R. S. G., F. A. M., and B. M. C. writing–original draft; F. A. M. and B. M. C. supervision; F. A. M. and B. M. C. funding acquisition.

Funding and additional information—This work was supported by grants from the National Health and Medical Research Council of Australia (NHMRC) (grant nos.: APP1138083 and APP1139316; to B. M. C. and F. A. M). B. M. C. is supported by an NHMRC investigator grant and previous senior research fellowship (grant nos.: APP2016410 and APP1136021). F. A. M. is supported by an

NHMRC Senior Research Fellowship (grant no.: APP1155794). T. P. W. is supported by an NHMRC Ideas Grant (grant no.: APP2010901) awarded to T. P. W. and F. A. M.

Conflict of interest—The authors declare that they have no conflicts of interest with the contents of this article.

Abbreviations—The abbreviations used are: AHM, α-helical motif; APP, amyloid precursor protein; ARF, ADP-ribosylation factor; CASK, Ca2+/calmodulin-dependent serine protein kinase; CID, CASK-interacting domain; co-IP, coimmunoprecipitation; DKO, double knockout; GST, glutathione-S-transferase; iPTM, interfacial PTM; ITC, isothermal titration calorimetry; MID, Munc18-1-interacting domain; Mint, Munc18-interacting protein; NMDA, N-methyl-d-aspartate; NRX1, neurexin-1; PAE, predicted alignment error; PDZbm, PDZ binding motif; PTB, phosphotyrosine binding; PTM, post-translational modification; SM, Sec1/Munc18; SNARE, soluble N-ethylmaleimide-sensitive factor attachment receptor; Sx1a, Syntaxin1a; TCEP, Tris(2-carboxyethyl)phosphine; TIRF, total internal reflection fluorescence; TJAP1, tight junction–associated protein 1.

References

1. Rogelj, B., Mitchell, J. C., Miller, C. C., and McLoughlin, D. M. (2006) The X11/Mint family of adaptor proteins. *Brain Res. Rev.* **52**, 305–315
2. Biederer, T., Cao, X., Sudhof, T. C., and Liu, X. (2002) Regulation of APP-dependent transcription complexes by Mint/X11s: differential functions of Mint isoforms. *J. Neurosci.* **22**, 7340–7351
3. Ho, C. S., Marinescu, V., Steinhilb, M. L., Gaut, J. R., Turner, R. S., and Stuenkel, E. L. (2002) Synergistic effects of Munc18a and X11 proteins on amyloid precursor protein metabolism. *J. Biol. Chem.* **277**, 27021–27028
4. Lee, J. H., Lau, K. F., Perkinton, M. S., Standen, C. L., Shemilt, S. J., Mercken, L., *et al.* (2003) The neuronal adaptor protein X11alpha reduces Abeta levels in the brains of Alzheimer's APPswe Tg2576 transgenic mice. *J. Biol. Chem.* **278**, 47025–47029
5. Motodate, R., Saito, Y., Hata, S., and Suzuki, T. (2016) Expression and localization of X11 family proteins in neurons. *Brain Res.* **1646**, 227–234
6. Tomita, S., Ozaki, T., Taru, H., Oguchi, S., Takeda, S., Yagi, Y., *et al.* (1999) Interaction of a neuron-specific protein containing PDZ domains with Alzheimer's amyloid precursor protein. *J. Biol. Chem.* **274**, 2243–2254
7. Borg, J. P., Ooi, J., Levy, E., and Margolis, B. (1996) The phosphotyrosine interaction domains of X11 and FE65 bind to distinct sites on the YENPTY motif of amyloid precursor protein. *Mol. Cell. Biol.* **16**, 6229–6241
8. Borg, J. P., Straight, S. W., Kaech, S. M., de Taddeo-Borg, M., Kroon, D. E., Karnak, D., *et al.* (1998) Identification of an evolutionarily conserved heterotrimeric protein complex involved in protein targeting. *J. Biol. Chem.* **273**, 31633–31636
9. Caster, A. H., and Kahn, R. A. (2013) Recruitment of the Mint3 adaptor is necessary for export of the amyloid precursor protein (APP) from the Golgi complex. *J. Biol. Chem.* **288**, 28567–28580
10. Chaufty, J., Sullivan, S. E., and Ho, A. (2012) Intracellular amyloid precursor protein sorting and amyloid-beta secretion are regulated by Src-mediated phosphorylation of Mint2. *J. Neurosci.* **32**, 9613–9625
11. Ho, A., Liu, X., and Sudhof, T. C. (2008) Deletion of Mint proteins decreases amyloid production in transgenic mouse models of Alzheimer's disease. *J. Neurosci.* **28**, 14392–14400
12. Matos, M. F., Xu, Y., Dulubova, I., Otwinowski, Z., Richardson, J. M., Tomchick, D. R., *et al.* (2012) Autoinhibition of Mint1 adaptor protein regulates amyloid precursor protein binding and processing. *Proc. Natl. Acad. Sci. U. S. A.* **109**, 3802–3807
13. Saito, Y., Akiyama, M., Araki, Y., Sumioka, A., Shiono, M., Taru, H., *et al.* (2011) Intracellular trafficking of the amyloid beta-protein precursor (APP) regulated by novel function of X11-like. *PLoS One* **6**, e22108
14. Sakuma, M., Tanaka, E., Taru, H., Tomita, S., Gandy, S., Nairn, A. C., *et al.* (2009) Phosphorylation of the amino-terminal region of X11L regulates its interaction with APP. *J. Neurochem.* **109**, 465–475
15. Sullivan, S. E., Dillon, G. M., Sullivan, J. M., and Ho, A. (2014) Mint proteins are required for synaptic activity-dependent amyloid precursor protein (APP) trafficking and amyloid beta generation. *J. Biol. Chem.* **289**, 15374–15383
16. Xie, X., Yan, X., Wang, Z., Zhou, H., Diao, W., Zhou, W., *et al.* (2013) Open-closed motion of Mint2 regulates APP metabolism. *J. Mol. Cell Biol.* **5**, 48–56
17. Zhang, Y., Wang, Y. G., Zhang, Q., Liu, X. J., Liu, X., Jiao, L., *et al.* (2009) Interaction of Mint2 with TrkA is involved in regulation of nerve growth factor-induced neurite outgrowth. *J. Biol. Chem.* **284**, 12469–12479
18. Zhang, Z., Lee, C. H., Mandiyan, V., Borg, J. P., Margolis, B., Schlessinger, J., *et al.* (1997) Sequence-specific recognition of the internalization motif of the Alzheimer's amyloid precursor protein by the X11 PTB domain. *EMBO J.* **16**, 6141–6150
19. Biederer, T., and Sudhof, T. C. (2000) Mints as adaptors. Direct binding to neurexins and recruitment of munc18. *J. Biol. Chem.* **275**, 39803–39806
20. Gotthardt, M., Trommsdorff, M., Nevitt, M. F., Shelton, J., Richardson, J. A., Stockinger, W., *et al.* (2000) Interactions of the low density lipoprotein receptor gene family with cytosolic adaptor and scaffold proteins suggest diverse biological functions in cellular communication and signal transduction. *J. Biol. Chem.* **275**, 25616–25624
21. Jones, K. A., Eng, A. G., Raval, P., Srivastava, D. P., and Penzes, P. (2014) Scaffold protein X11alpha interacts with kalirin-7 in dendrites and recruits it to Golgi outposts. *J. Biol. Chem.* **289**, 35517–35529
22. Minami, S. S., Sung, Y. M., Dumanis, S. B., Chi, S. H., Burns, M. P., Ann, E. J., *et al.* (2010) The cytoplasmic adaptor protein X11alpha and extracellular matrix protein Reelin regulate ApoE receptor 2 trafficking and cell movement. *FASEB J.* **24**, 58–69
23. Motodate, R., Saito, H., Sobu, Y., Hata, S., Saito, Y., Nakaya, T., *et al.* (2019) X11 and X11-like proteins regulate the level of extrasynaptic glutamate receptors. *J. Neurochem.* **148**, 480–498
24. Stafford, R. L., Ear, J., Knight, M. J., and Bowie, J. U. (2011) The molecular basis of the Caskin1 and Mint1 interaction with CASK. *J. Mol. Biol.* **412**, 3–13
25. Tabuchi, K., Biederer, T., Butz, S., and Sudhof, T. C. (2002) CASK participates in alternative tripartite complexes in which Mint 1 competes for binding with caskin 1, a novel CASK-binding protein. *J. Neurosci.* **22**, 4264–4273
26. Wu, X., Cai, Q., Chen, Y., Zhu, S., Mi, J., Wang, J., *et al.* (2020) Structural basis for the high-affinity interaction between CASK and Mint1. *Structure* **28**, 664–673.e3
27. Zhang, Z., Li, W., Yang, G., Lu, X., Qi, X., Wang, S., *et al.* (2020) CASK modulates the assembly and function of the Mint1/Munc18-1 complex to regulate insulin secretion. *Cell Discov.* **6**, 92
28. Graham, M. E., Prescott, G. R., Johnson, J. R., Jones, M., Walmesley, A., Haynes, L. P., *et al.* (2011) Structure-function study of mammalian Munc18-1 and C. elegans UNC-18 implicates domain 3b in the regulation of exocytosis. *PLoS One* **6**, e17999
29. Han, G. A., Park, S., Bin, N. R., Jung, C. H., Kim, B., Chandrasegaram, P., *et al.* (2014) A pivotal role for pro-335 in balancing the dual functions of Munc18-1 domain-3a in regulated exocytosis. *J. Biol. Chem.* **289**, 33617–33628
30. Okamoto, M., and Sudhof, T. C. (1997) Mints, Munc18-interacting proteins in synaptic vesicle exocytosis. *J. Biol. Chem.* **272**, 31459–31464
31. Okamoto, M., and Sudhof, T. C. (1998) Mint 3: a ubiquitous mint isoform that does not bind to munc18-1 or -2. *Eur. J. Cell Biol.* **77**, 161–165
32. Park, J. H., Jung, M. S., Kim, Y. S., Song, W. J., and Chung, S. H. (2012) Phosphorylation of Munc18-1 by Dyrk1A regulates its interaction with syntaxin 1 and X11alpha. *J. Neurochem.* **122**, 1081–1091

33. Ho, A., Morishita, W., Hammer, R. E., Malenka, R. C., and Sudhof, T. C. (2003) A role for Mints in transmitter release: Mint 1 knockout mice exhibit impaired GABAergic synaptic transmission. *Proc. Natl. Acad. Sci. U. S. A.* **100**, 1409–1414
34. Sano, Y., Syuzo-Takabatake, A., Nakaya, T., Saito, Y., Tomita, S., Itohara, S., *et al.* (2006) Enhanced amyloidogenic metabolism of the amyloid beta-protein precursor in the X11L-deficient mouse brain. *J. Biol. Chem.* **281**, 37853–37860
35. Gross, G. G., Lone, G. M., Leung, L. K., Hartenstein, V., and Guo, M. (2013) X11/Mint genes control polarized localization of axonal membrane proteins *in vivo*. *J. Neurosci.* **33**, 8575–8586
36. Kondo, M., Shiono, M., Itoh, G., Takei, N., Matsushima, T., Maeda, M., *et al.* (2010) Increased amyloidogenic processing of transgenic human APP in X11-like deficient mouse brain. *Mol. Neurodegener.* **5**, 35
37. Saluja, I., Paulson, H., Gupta, A., and Turner, R. S. (2009) X11alpha haploinsufficiency enhances Abeta amyloid deposition in Alzheimer's disease transgenic mice. *Neurobiol. Dis.* **36**, 162–168
38. Lanoue, V., Chai, Y. J., Brouillet, J. Z., Weckhuysen, S., Palmer, E. E., Collins, B. M., *et al.* (2019) STXBP1 encephalopathy: connecting neurodevelopmental disorders with alpha-synucleinopathies? *Neurology* **93**, 114–123
39. Verhage, M., and Sorensen, J. B. (2020) SNAREopathies: diversity in mechanisms and symptoms. *Neuron* **107**, 22–37
40. Hayashi, S., Uehara, D. T., Tanimoto, K., Mizuno, S., Chinen, Y., Fukumura, S., *et al.* (2017) Comprehensive investigation of CASK mutations and other genetic etiologies in 41 patients with intellectual disability and microcephaly with pontine and cerebellar hypoplasia (MICPCH). *PLoS One* **12**, e0181791
41. Hsueh, Y. P. (2009) Calcium/calmodulin-dependent serine protein kinase and mental retardation. *Ann. Neurol.* **66**, 438–443
42. LaConte, L. E. W., Chavan, V., DeLuca, S., Rubin, K., Malc, J., Berry, S., *et al.* (2019) An N-terminal heterozygous missense CASK mutation is associated with microcephaly and bilateral retinal dystrophy plus optic nerve atrophy. *Am. J. Med. Genet. A* **179**, 94–103
43. Piluso, G., D'Amico, F., Saccone, V., Bismuto, E., Rotundo, I. L., Di Domenico, M., *et al.* (2009) A missense mutation in CASK causes FG syndrome in an Italian family. *Am. J. Hum. Genet.* **84**, 162–177
44. Peycheva, V., Kamenarova, K., Ivanova, N., Stamatov, D., Avdjieva-Tzavella, D., Alexandrova, I., *et al.* (2018) Chromosomal microarray analysis of Bulgarian patients with epilepsy and intellectual disability. *Gene* **667**, 45–55
45. Babatz, T. D., Kumar, R. A., Sudi, J., Dobyns, W. B., and Christian, S. L. (2009) Copy number and sequence variants implicate APBA2 as an autism candidate gene. *Autism Res.* **2**, 359–364
46. Lin, A. Y., Henry, S., Reissner, C., Neupert, C., Kenny, C., Missler, M., *et al.* (2019) A rare autism-associated MINT2/APBA2 mutation disrupts neurexin trafficking and synaptic function. *Sci. Rep.* **9**, 6024
47. Li, W., Xing, Y., Wang, Y., Xu, T., Song, E., and Feng, W. (2023) A non-canonical target-binding site in Munc18-1 domain 3b for assembling the Mint1-Munc18-1-syntaxin-1 complex. *Structure* **31**, 68–77.e5
48. Lee, H. Y., Park, J. B., Jang, I. H., Chae, Y. C., Kim, J. H., Kim, I. S., *et al.* (2004) Munc-18-1 inhibits phospholipase D activity by direct interaction in an epidermal growth factor-reversible manner. *J. Biol. Chem.* **279**, 16339–16348
49. Okamoto, M., and Südhof, T. C. (1997) Mints, Munc18-interacting proteins in synaptic vesicle exocytosis. *J. Biol. Chem.* **272**, 31459–31464
50. Diella, F., Haslam, N., Chica, C., Budd, A., Michael, S., Brown, N. P., *et al.* (2008) Understanding eukaryotic linear motifs and their role in cell signaling and regulation. *Front. Biosci.* **13**, 6580–6603
51. Hornbeck, P. V., Zhang, B., Murray, B., Kornhauser, J. M., Latham, V., and Skrzypek, E. (2015) PhosphoSitePlus, 2014: mutations, PTMs and recalibrations. *Nucleic Acids Res.* **43**, D512–D520
52. Dunning, C. J., Black, H. L., Andrews, K. L., Davenport, E. C., Conboy, M., Chawla, S., *et al.* (2016) Multisite tyrosine phosphorylation of the N-terminus of Mint1/X11alpha by Src kinase regulates the trafficking of amyloid precursor protein. *J. Neurochem.* **137**, 518–527
53. [preprint] Evans, R., O'Neill, M., Pritzel, A., Antropova, N., Senior, A., Green, T., *et al.* (2022) Protein complex prediction with AlphaFold-multimer. *bioRxiv*. https://doi.org/10.1101/2021.10.04.463034
54. Jumper, J., Evans, R., Pritzel, A., Green, T., Figurnov, M., Ronneberger, O., *et al.* (2021) Highly accurate protein structure prediction with AlphaFold. *Nature* **596**, 583–589
55. [preprint] Ko, J., and Lee, J. (2021) Can AlphaFold2 predict protein-peptide complex structures accurately?. *bioRxiv*. https://doi.org/10.1101/2021.07.27.453972
56. Poetz, F., Corbo, J., Levdansky, Y., Spiegelhalter, A., Lindner, D., Magg, V., *et al.* (2021) RNF219 attenuates global mRNA decay through inhibition of CCR4-NOT complex-mediated deadenylation. *Nat. Commun.* **12**, 7175
57. [preprint] Simonetti, B., Guo, Q., Gimenez-Andres, M., Chen, K.-E., Moody, E. R. R., Evans, A. J., *et al.* (2021) Mechanistic basis for SNX27-retromer coupling to ESCPE-1 in promoting endosomal cargo recycling. *bioRxiv*. https://doi.org/10.1101/2021.08.28.457928
58. [preprint] Tsaban, T., Varga, J., Avraham, O., Ben-Aharon, Z., Khramushin, A., and Schueler-Furman, O. (2021) Harnessing protein folding neural networks for peptide-protein docking. *bioRxiv*. https://doi.org/10.1101/2021.08.01.454656
59. Mirdita, M., Schutze, K., Moriwaki, Y., Heo, L., Ovchinnikov, S., and Steinegger, M. (2022) ColabFold: making protein folding accessible to all. *Nat. Methods* **19**, 679–682
60. [preprint] Jiang, A., Gormal, R. S., Kasula, R., Blum, A., Salla-Martret, M., Chai, Y. J., *et al.* (2023) VAMP2/Munc18-1 domain 3a interaction controls the nanoscale reorganization underpinning vesicular priming. *bioRxiv*. https://doi.org/10.1101/2023.09.10.556776
61. Peleg, Y., Vincentelli, R., Collins, B. M., Chen, K. E., Livingstone, E. K., Weeratunga, S., *et al.* (2021) Community-wide experimental evaluation of the PROSS stability-design method. *J. Mol. Biol.* **433**, 166964
62. Stepien, K. P., Xu, J., Zhang, X., Bai, X. C., and Rizo, J. (2022) SNARE assembly enlightened by cryo-EM structures of a synaptobrevin-Munc18-1-syntaxin-1 complex. *Sci. Adv.* **8**, eabo5272
63. Baker, R. W., Jeffrey, P. D., Zick, M., Phillips, B. P., Wickner, W. T., and Hughson, F. M. (2015) A direct role for the Sec1/Munc18-family protein Vps33 as a template for SNARE assembly. *Science* **349**, 1111–1114
64. Han, G. A., Bin, N. R., Kang, S. Y., Han, L., and Sugita, S. (2013) Domain 3a of Munc18-1 plays a crucial role at the priming stage of exocytosis. *J. Cell Sci.* **126**, 2361–2371
65. Kasula, R., Chai, Y. J., Bademosi, A. T., Harper, C. B., Gormal, R. S., Morrow, I. C., *et al.* (2016) The Munc18-1 domain 3a hinge-loop controls syntaxin-1A nanodomain assembly and engagement with the SNARE complex during secretory vesicle priming. *J. Cell Biol.* **214**, 847–858
66. Martin, S., Tomatis, V. M., Papadopulos, A., Christie, M. P., Malintan, N. T., Gormal, R. S., *et al.* (2013) The Munc18-1 domain 3a loop is essential for neuroexocytosis but not for syntaxin-1A transport to the plasma membrane. *J. Cell Sci.* **126**, 2353–2360
67. Burkhardt, P., Hattendorf, D. A., Weis, W. I., and Fasshauer, D. (2008) Munc18a controls SNARE assembly through its interaction with the syntaxin N-peptide. *EMBO J.* **27**, 923–933
68. Burkhardt, P., Stegmann, C. M., Cooper, B., Kloepper, T. H., Imig, C., Varoqueaux, F., *et al.* (2011) Primordial neurosecretory apparatus identified in the choanoflagellate Monosiga brevicollis. *Proc. Natl. Acad. Sci. U. S. A.* **108**, 15264–15269
69. Bracher, A., Perrakis, A., Dresbach, T., Betz, H., and Weissenhorn, W. (2000) The X-ray crystal structure of neuronal Sec1 from squid sheds new light on the role of this protein in exocytosis. *Struct. Fold Des.* **8**, 685–694
70. Bracher, A., and Weissenhorn, W. (2001) Crystal structures of neuronal squid Sec1 implicate inter-domain hinge movement in the release of t-SNAREs. *J. Mol. Biol.* **306**, 7–13
71. Hu, S. H., Christie, M. P., Saez, N. J., Latham, C. F., Jarrott, R., Lua, L. H., *et al.* (2011) Possible roles for Munc18-1 domain 3a and Syntaxin1 N-peptide and C-terminal anchor in SNARE complex formation. *Proc. Natl. Acad. Sci. U. S. A.* **108**, 1040–1045
72. Oughtred, R., Rust, J., Chang, C., Breitkreutz, B. J., Stark, C., Willems, A., *et al.* (2021) The BioGRID database: a comprehensive biomedical resource of curated protein, genetic, and chemical interactions. *Protein Sci.* **30**, 187–200

73. Sifri, C., Hoeg, L., Durocher, D., and Setiaputra, D. (2023) An AlphaFold2 map of the 53BP1 pathway identifies a direct SHLD3-RIF1 interaction critical for shieldin activity. *EMBO Rep.* **24**, e56834
74. He, X., Cooley, K., Chung, C. H., Dashti, N., and Tang, J. (2007) Apolipoprotein receptor 2 and X11 alpha/beta mediate apolipoprotein E-induced endocytosis of amyloid-beta precursor protein and beta-secretase, leading to amyloid-beta production. *J. Neurosci.* **27**, 4052–4060
75. Araki, Y., Tomita, S., Yamaguchi, H., Miyagi, N., Sumioka, A., Kirino, Y., *et al.* (2003) Novel cadherin-related membrane proteins, alcadeins, enhance the X11-like protein-mediated stabilization of amyloid beta-protein precursor metabolism. *J. Biol. Chem.* **278**, 49448–49458
76. Leonoudakis, D., Conti, L. R., Radeke, C. M., McGuire, L. M., and Vandenberg, C. A. (2004) A multiprotein trafficking complex composed of SAP97, CASK, Veli, and Mint1 is associated with inward rectifier Kir2 potassium channels. *J. Biol. Chem.* **279**, 19051–19063
77. Huttlin, E. L., Bruckner, R. J., Navarrete-Perea, J., Cannon, J. R., Baltier, K., Gebreab, F., *et al.* (2021) Dual proteome-scale networks reveal cell-specific remodeling of the human interactome. *Cell* **184**, 3022–3040.e8
78. Hill, K., Li, Y., Bennett, M., McKay, M., Zhu, X., Shern, J., *et al.* (2003) Munc18 interacting proteins: ADP-ribosylation factor-dependent coat proteins that regulate the traffic of beta-Alzheimer's precursor protein. *J. Biol. Chem.* **278**, 36032–36040
79. Lee, Y., Kim, B. S., Choi, S., Lee, E. Y., Park, S., Hwang, J., *et al.* (2019) Makes caterpillars floppy-like effector-containing MARTX toxins require host ADP-ribosylation factor (ARF) proteins for systemic pathogenicity. *Proc. Natl. Acad. Sci. U. S. A.* **116**, 18031–18040
80. Bai, G., Li, H., Qin, P., Guo, Y., Yang, W., Lian, Y., *et al.* (2023) Ca2+-induced release of IQSEC2/BRAG1 autoinhibition under physiological and pathological conditions. *J. Cell Biol.* **222**, e202307117
81. Peurois, F., Veyron, S., Ferrandez, Y., Ladid, I., Benabdi, S., Zeghouf, M., *et al.* (2017) Characterization of the activation of small GTPases by their GEFs on membranes using artificial membrane tethering. *Biochem. J.* **474**, 1259–1272
82. Um, J. W. (2017) Synaptic functions of the IQSEC family of ADP-ribosylation factor guanine nucleotide exchange factors. *Neurosci. Res.* **116**, 54–59
83. Ansar, M., Chung, H. L., Al-Otaibi, A., Elagabani, M. N., Ravenscroft, T. A., Paracha, S. A., *et al.* (2019) Bi-allelic variants in IQSEC1 cause intellectual disability, developmental delay, and short stature. *Am. J. Hum. Genet.* **105**, 907–920
84. Zerem, A., Haginoya, K., Lev, D., Blumkin, L., Kivity, S., Linder, I., *et al.* (2016) The molecular and phenotypic spectrum of IQSEC2-related epilepsy. *Epilepsia* **57**, 1858–1869
85. Scholz, R., Berberich, S., Rathgeber, L., Kolleker, A., Köhr, G., and Kornau, H. C. (2010) AMPA receptor signaling through BRAG2 and Arf6 critical for long-term synaptic depression. *Neuron* **66**, 768–780
86. Mardones, G. A., Burgos, P. V., Lin, Y., Kloer, D. P., Magadan, J. G., Hurley, J. H., *et al.* (2013) Structural basis for the recognition of tyrosine-based sorting signals by the mu3A subunit of the AP-3 adaptor complex. *J. Biol. Chem.* **288**, 9563–9571
87. Sanger, A., Hirst, J., Davies, A. K., and Robinson, M. S. (2019) Adaptor protein complexes and disease at a glance. *J. Cell Sci.* **132**, jcs222992
88. Hung, A. Y., and Sheng, M. (2002) PDZ domains: structural modules for protein complex assembly. *J. Biol. Chem.* **277**, 5699–5702
89. Nourry, C., Grant, S. G., and Borg, J. P. (2003) PDZ domain proteins: plug and play! *Sci. STKE* **2003**, RE7
90. Long, J. F., Feng, W., Wang, R., Chan, L. N., Ip, F. C., Xia, J., *et al.* (2005) Autoinhibition of X11/Mint scaffold proteins revealed by the closed conformation of the PDZ tandem. *Nat. Struct. Mol. Biol.* **12**, 722–728
91. Burke, D. F., Bryant, P., Barrio-Hernandez, I., Memon, D., Pozzati, G., Shenoy, A., *et al.* (2023) Towards a structurally resolved human protein interaction network. *Nat. Struct. Mol. Biol.* **30**, 216–225
92. Gao, M., Nakajima An, D., Parks, J. M., and Skolnick, J. (2022) AF2Complex predicts direct physical interactions in multimeric proteins with deep learning. *Nat. Commun.* **13**, 1744
93. Gao, M., Nakajima An, D., and Skolnick, J. (2022) Deep learning-driven insights into super protein complexes for outer membrane protein biogenesis in bacteria. *Elife* **11**, e82885
94. Humphreys, I. R., Pei, J., Baek, M., Krishnakumar, A., Anishchenko, I., Ovchinnikov, S., *et al.* (2021) Computed structures of core eukaryotic protein complexes. *Science* **374**, eabm4805
95. Yu, D., Chojnowski, G., Rosenthal, M., and Kosinski, J. (2023) AlphaPulldown-a python package for protein-protein interaction screens using AlphaFold-Multimer. *Bioinformatics* **39**, btac749
96. Maximov, A., Sudhof, T. C., and Bezprozvanny, I. (1999) Association of neuronal calcium channels with modular adaptor proteins. *J. Biol. Chem.* **274**, 24453–24456
97. Penzes, P., Johnson, R. C., Sattler, R., Zhang, X., Huganir, R. L., Kambampati, V., *et al.* (2001) The neuronal Rho-GEF Kalirin-7 interacts with PDZ domain-containing proteins and regulates dendritic morphogenesis. *Neuron* **29**, 229–242
98. Dean, C., and Dresbach, T. (2006) Neuroligins and neurexins: linking cell adhesion, synapse formation and cognitive function. *Trends Neurosci.* **29**, 21–29
99. Tamaki, H., Sanda, M., Katsumata, O., Hara, Y., Fukaya, M., and Sakagami, H. (2012) Pilt is a coiled-coil domain-containing protein that localizes at the trans-Golgi complex and regulates its structure. *FEBS Lett.* **586**, 3064–3070
100. Kawabe, H., Nakanishi, H., Asada, M., Fukuhara, A., Morimoto, K., Takeuchi, M., *et al.* (2001) Pilt, a novel peripheral membrane protein at tight junctions in epithelial cells. *J. Biol. Chem.* **276**, 48350–48355
101. Ye, F., Zeng, M., and Zhang, M. (2018) Mechanisms of MAGUK-mediated cellular junctional complex organization. *Curr. Opin. Struct. Biol.* **48**, 6–15
102. Kondo, Y., Hanai, A., Nakai, W., Katoh, Y., Nakayama, K., and Shin, H. W. (2012) ARF1 and ARF3 are required for the integrity of recycling endosomes and the recycling pathway. *Cell Struct. Funct.* **37**, 141–154
103. Nakai, W., Kondo, Y., Saitoh, A., Naito, T., Nakayama, K., and Shin, H. W. (2013) ARF1 and ARF4 regulate recycling endosomal morphology and retrograde transport from endosomes to the Golgi apparatus. *Mol. Biol. Cell* **24**, 2570–2581
104. Fasano, G., Muto, V., Radio, F. C., Venditti, M., Mosaddeghzadeh, N., Coppola, S., *et al.* (2022) Dominant ARF3 variants disrupt Golgi integrity and cause a neurodevelopmental disorder recapitulated in zebrafish. *Nat. Commun.* **13**, 6841
105. Sakamoto, M., Sasaki, K., Sugie, A., Nitta, Y., Kimura, T., Gursoy, S., *et al.* (2021) De novo ARF3 variants cause neurodevelopmental disorder with brain abnormality. *Hum. Mol. Genet.* **31**, 69–81
106. Blumstein, J., Faundez, V., Nakatsu, F., Saito, T., Ohno, H., and Kelly, R. B. (2001) The neuronal form of adaptor protein-3 is required for synaptic vesicle formation from endosomes. *J. Neurosci.* **21**, 8034–8042
107. Evstratova, A., Chamberland, S., Faundez, V., and Toth, K. (2014) Vesicles derived via AP-3-dependent recycling contribute to asynchronous release and influence information transfer. *Nat. Commun.* **5**, 5530
108. Li, P., Merrill, S. A., Jorgensen, E. M., and Shen, K. (2016) Two clathrin adaptor protein complexes instruct axon-dendrite polarity. *Neuron* **90**, 564–580
109. Newell-Litwa, K., Chintala, S., Jenkins, S., Pare, J. F., McGaha, L., Smith, Y., *et al.* (2010) Hermansky-Pudlak protein complexes, AP-3 and BLOC-1, differentially regulate presynaptic composition in the striatum and hippocampus. *J. Neurosci.* **30**, 820–831
110. Seong, E., Wainer, B. H., Hughes, E. D., Saunders, T. L., Burmeister, M., and Faundez, V. (2005) Genetic analysis of the neuronal and ubiquitous AP-3 adaptor complexes reveals divergent functions in brain. *Mol. Biol. Cell* **16**, 128–140
111. Shetty, A., Sytnyk, V., Leshchyns'ka, I., Puchkov, D., Haucke, V., and Schachner, M. (2013) The neural cell adhesion molecule promotes maturation of the presynaptic endocytotic machinery by switching synaptic vesicle recycling from adaptor protein 3 (AP-3)- to AP-2-dependent mechanisms. *J. Neurosci.* **33**, 16828–16845
112. Voglmaier, S. M., Kam, K., Yang, H., Fortin, D. L., Hua, Z., Nicoll, R. A., *et al.* (2006) Distinct endocytic pathways control the rate and extent of synaptic vesicle protein recycling. *Neuron* **51**, 71–84

113. Ammann, S., Schulz, A., Krageloh-Mann, I., Dieckmann, N. M., Niethammer, K., Fuchs, S., *et al.* (2016) Mutations in AP3D1 associated with immunodeficiency and seizures define a new type of Hermansky-Pudlak syndrome. *Blood* **127**, 997–1006
114. Assoum, M., Philippe, C., Isidor, B., Perrin, L., Makrythanasis, P., Sondheimer, N., *et al.* (2016) Autosomal-recessive mutations in AP3B2, adaptor-related protein complex 3 beta 2 subunit, cause an early-onset epileptic encephalopathy with optic atrophy. *Am. J. Hum. Genet.* **99**, 1368–1376
115. Miesenbock, G., De Angelis, D. A., and Rothman, J. E. (1998) Visualizing secretion and synaptic transmission with pH-sensitive green fluorescent proteins. *Nature* **394**, 192–195
116. Kubala, M. H., Kovtun, O., Alexandrov, K., and Collins, B. M. (2010) Structural and thermodynamic analysis of the GFP:GFP-nanobody complex. *Protein Sci.* **19**, 2389–2401
117. Papadopulos, A., Martin, S., Tomatis, V. M., Gormal, R. S., and Meunier, F. A. (2013) Secretagogue stimulation of neurosecretory cells elicits filopodial extensions uncovering new functional release sites. *J. Neurosci.* **33**, 19143–19153
118. Mirdita, M., Steinegger, M., and Soding, J. (2019) MMseqs2 desktop and local web server app for fast, interactive sequence searches. *Bioinformatics* **35**, 2856–2858
119. Hornak, V., Abel, R., Okur, A., Strockbine, B., Roitberg, A., and Simmerling, C. (2006) Comparison of multiple Amber force fields and development of improved protein backbone parameters. *Proteins* **65**, 712–725
120. Ashkenazy, H., Abadi, S., Martz, E., Chay, O., Mayrose, I., Pupko, T., *et al.* (2016) ConSurf 2016: an improved methodology to estimate and visualize evolutionary conservation in macromolecules. *Nucleic Acids Res.* **44**, W344–W350